Temperatures since the last glacial maximum in the Maritime Alps recorded by cosmogenic noble gases

Marissa M. Tremblay[1,2,*], David L. Shuster[1,2], Matteo Spagnolo[3], Hans Renssen[4], Adriano Ribolini[5]

[1]Department of Earth and Planetary Science, University of California, Berkeley, Berkeley, CA, 94720-4767 USA

[2]Berkeley Geochronology Center, Berkeley, CA, 94709, USA

[3]Department of Geography and Environment, School of Geosciences, University of Aberdeen, Aberdeen, AB24 3UF, UK

[4]Department of Natural Sciences and Environmental Health, University College of Southeast Norway, 3800 Bø, Norway

[5]Dipartimento di Scienze della Terra, Universita' di Pisa, 56126 Italy.

[*]Now located at Scottish Universities Environmental Research Centre, Rankine Avenue, East Kilbride, G75 0QF, UK

Correspondence to: Marissa M. Tremblay (marissa.tremblay@glasgow.ac.uk)

ABSTRACT

While proxy records have been used to reconstruct late Quaternary climate parameters throughout the European Alps, our knowledge of deglacial climate conditions in the Maritime Alps is limited. Here, we utilize a new and independent geochemical technique–cosmogenic noble gas paleothermometry–to investigate temperatures in the Maritime Alps since the last glacial maximum (LGM). We measured cosmogenic ^{3}He in quartz from boulders in nested moraines in the Gesso Valley, Italy. Paired with cosmogenic ^{10}Be measurements and ^{3}He diffusion experiments on quartz from the same boulders, the cosmogenic ^{3}He abundances record the temperatures these boulders experienced during their exposure. We calculate effective diffusion temperatures (EDTs) over the last ~22 ka ranging from 8 to 25ºC. These EDTs, which are functionally related to, but greater than, mean ambient temperatures, are consistent with temperatures inferred from other proxies in nearby Alpine regions and those predicted by a transient general circulation model. In detail, however, we also find different EDTs for boulders from the same moraines, thus limiting the resolution of the temperature reconstruction. We explore possible causes for these intra-moraine discrepancies including variations in radiative heating, our treatment of complex helium diffusion, uncertainties in our grain size analyses, and unaccounted for erosion or cosmogenic inheritance.

KEYWORDS

cosmogenic isotopes; paleoclimate; Quaternary; Europe

INTRODUCTION

Data from paleoclimate proxies constrain the dynamics of Earth's climate system on timescales inaccessible with the instrumental record. Proxy observations from key intervals of Earth's past climate, such as the last glacial maximum (LGM) and subsequent deglaciation, allow us to understand how the climate system responds to a change in forcing (e.g., Annan and Hargreaves, 2013; Schmittner et al., 2011; von der Heydt et al., 2016) and evaluate the ability of climate models to simulate the climate system's response (e.g., Annan and Hargreaves, 2015; Harrison et al., 2015; Schmidt et al., 2014) both of which improve our ability to forecast future climate change (e.g., Masson-Delmotte et al., 2013). Terrestrial proxies are particularly important for assessing how changes in large scale ocean-atmosphere dynamics manifest at a regional scale in the continental settings that people inhabit and depend upon.

An extensive network of terrestrial climate reconstructions since the last glacial maximum (LGM) exists across the European Alps from pollen, chironomids (midges), organic biomarkers, and inorganic isotope systems (e.g., Bartlein et al., 2011; Blaga et al., 2013; Heiri et al., 2014; Luetscher et al., 2015). Despite such an extensive proxy network, our knowledge of deglacial climate conditions in the southern sector of the French and Italian Alps (hereafter referred to as the Maritime Alps) from proxy records is limited. While there are a handful of pollen-based reconstructions from the Maritime Alps of climate parameters in the Holocene, such as mean temperature during the coldest month and mean annual precipitation (Bartlein et al., 2011; Cheddadi et al., 1996; Cheddadi and Bar-Hen, 2009; Davis et al., 2003; Wu et al., 2007), no reconstruction from the region extends back to the LGM. Similarly, there is only one reconstruction of mean July temperatures from fossil assemblages of chironomids proximal (<

100 km) to the Maritime Alps. This chironomid record from Lago Piccolo di Avigliana is temporal limited to 14–9.5 thousand years ago (Larocque and Finsinger, 2008). There are two proxy studies from the Maritime Alps that extend into the latest Pleistocene which we are aware of: one reporting pollen fossil assemblages in sixteen high elevation (> 1700 m) lakes (Brisset et al., 2015) and one reporting fossil chironomid assemblages from Lac Long Inférieur in France (Gandouin and Franquet, 2002). Unfortunately, neither of these studies interprets the proxies in terms of quantitative climate parameters.

Due to the Maritime Alps' (1) southerly latitude, (2) generally lower elevations and (3) proximity to the Mediterranean Sea, the late Quaternary climatic evolution and glacier dynamics in this region may have differed substantially from those in Alpine regions further north and further inland (e.g., Kuhlemann et al., 2008), despite the apparent synchronicity of glacier advances during the LGM and later stadials recorded by moraines across the Alps (e.g., Federici et al., 2017; Ivy-Ochs et al., 2007; Kuhlemann et al., 2008). Reconstructing temperatures in the Maritime Alps since the LGM would therefore fill a gap in an otherwise extensive network of proxy-based reconstructions of post-LGM climate across the Alps, and address the specific question of how climate evolution in the Maritime Alps during deglaciation may have differed from other Alpine sectors. For example, in combination with the positions and chronology of moraines, a well-resolved local temperature record could be used to inform a simple glacier mass balance model for valleys in the Maritime Alps during the deglacial period. With constraints on local deglacial temperatures, such a mass balance model could be used to crudely invert for changes in precipitation during deglaciation (e.g. Kessler et al., 2006). This paired temperature-precipitation reconstruction could then be compared to proxy records further north and inland in

91 the Alps to assess how climate and glacier dynamics varied across the region during deglaciation
92 (e.g., Becker et al., 2016).
93
94 In addition to assessing climatic variability during deglaciation across the European Alps,
95 temperature records from an independent proxy could provide needed tests of different
96 methodologies for reconstructing climate parameters over this time interval. Reconstructions of
97 climate parameters from existing proxies in the European Alps commonly exhibit significant
98 disagreement with climate model simulations prior to the Holocene. Pollen-based reconstructions
99 suggest much colder temperatures, particularly in the winter, than the models predict (e.g. Jost et
100 al., 2005), while models predict higher summertime temperatures than chironomid-based
101 reconstructions during interstadials (Heiri et al., 2014). It is unclear whether these disagreements
102 are attributable to limitations in the global climate models used to simulate paleoclimate, a
103 breakdown in the assumptions of biologically-based reconstructions, or some combination of
104 both. Having independent pre-Holocene temperature records in the European Alps that are
105 mechanistically governed by different processes would therefore help in assessing the cause of
106 the current proxy-model discrepancies.
107
108 Cosmogenic noble gas paleothermometry is a new geochemical technique for reconstructing past
109 Earth surface temperatures (Tremblay et al., 2014a). Cosmogenic nuclides are produced by
110 nuclear interactions between target atoms and high-energy cosmic-ray particles, both in Earth's
111 atmosphere and in the solid Earth. Because the flux of secondary cosmic-ray particles decreases
112 exponentially with depth in rock, production of cosmogenic nuclides is restricted to the
113 uppermost few meters of the Earth's crust. The near surface production of rare nuclides such as

^{10}Be and ^{26}Al by cosmic-ray particle interactions in common rock-forming minerals like quartz has been extensively developed and utilized over the last 25 years by the geomorphology community to date the surface exposure of rocks and quantify erosion rates (e.g., Granger et al., 2013). Rare noble gas nuclides such as ^{3}He and ^{21}Ne are also produced in minerals by cosmic-ray particle interactions. In common minerals like quartz and feldspars, these noble gases sometimes exhibit diffusive loss at Earth surface temperatures (Gourbet et al., 2012; Shuster and Farley, 2005; Tremblay et al., 2017, 2014b) and thus have not been widely utilized in cosmogenic nuclide studies. However, cosmogenic noble gas–mineral pairs exhibiting open-system behavior (simultaneous production and diffusion) can be utilized to reconstruct the temperatures that rocks experience while exposed to cosmic-ray particles at Earth's surface when paired with observations of a quantitatively retained cosmogenic nuclide. In high latitude and/or high altitude environments, theoretical calculations indicate that measurements of ^{3}He in quartz can record temperature variations from the last glacial period to the present (Tremblay et al., 2014a).

Here, we apply cosmogenic noble gas paleothermometry to investigate temperatures since the last glacial maximum (LGM) in the Gesso Valley, located in the southernmost Maritime Alps of Italy approximately 40 km from the Gulf of Genoa in the Mediterranean Sea (Fig. 1). The Gesso Valley was glaciated during the last glacial period. Glacial moraines and other geomorphic features have been mapped throughout the basin (Federici et al., 2003), and cosmogenic ^{10}Be exposure ages have been determined for boulders from three nested moraines that span from the LGM to the Younger Dryas cold period (YD) (Federici et al., 2017, 2012, 2008). A number of younger, Holocene-age moraines are preserved at higher elevations in the Gesso Valley (Fig. 1),

and small glaciers restricted to the highest elevation cirques persist today (Federici et al., 2017). We measured cosmogenic ^{3}He abundances in quartz from a subset of the boulders with ^{10}Be exposure ages from the three previously-studied moraines. We also conducted stepwise degassing experiments to quantify the kinetics of ^{3}He diffusion in quartz from these boulders. Because cosmogenic ^{3}He is simultaneously produced and diffusively lost during exposure in the moraines, the 'apparent' exposure ages we calculate from the measured ^{3}He abundances are younger than the 'true' exposure age determined from the ^{10}Be measurements. The difference between the 'apparent' and 'true' exposure ages can be used to calculate the integrated effective diffusion temperature (EDT) during exposure. This integrated EDT is the temperature corresponding to the mean diffusivity over a variable temperature history, and is therefore a direct function of the ambient temperature history (Tremblay et al., 2014a). Paired with sample-specific ^{3}He diffusion kinetics, we use the difference between 'apparent' and 'true' exposure ages to model the permissible integrated EDTs, and by relation ambient temperature histories, of each boulder. The presence of numerous moraines with different exposure ages within the same valley is advantageous because it allows us to reconstruct temperatures over different time intervals for an area with a shared climate history.

Existing constraints on the late Quaternary climate of the Maritime Alps

Here we briefly review the existing proxy- and model-based constraints on climate conditions since the LGM in the Maritime Alps; a complete overview of proxy records for the entire European Alps is beyond the scope of this paper. Over the historical period, the Maritime Alps have been characterized by warmer mean annual temperatures (MAT), smaller annual temperature amplitudes, lower mean annual precipitation (MAP), and snow cover that is thinner

and lasts for a smaller fraction of the year than in other Alpine sectors (Durand et al., 2009a, 2009b). The Maritime Alps most likely remained the warmest Alpine sector during the late Quaternary, given that the Maritime Alps are ~6º south of the northernmost eastern Alps, and thus would have experienced greater insolation and generally higher temperatures during this time period. Warmer overall conditions is consistent with species distribution and phylogeographical models, which suggest that the Maritime Alps remained warmer than other parts of the Alps and functioned as a refugium for plant species during the last glacial period (Casazza et al., 2016). However, temperature and precipitation anomalies in the Maritime Alps during specific climatic intervals of the late Quaternary may have been distinct from other Alpine sectors. For example, during the Mid-Holocene Warm period 6,000 years ago, pollen-based reconstructions indicate that Maritime Alps winters may have been as much as 2–3 ºC colder than today, while throughout the rest of the Alps winter temperatures were comparable to today (Bartlein et al., 2011; Cheddadi et al., 1996; Wu et al., 2007). For the same time period, pollen-based reconstructions indicate that the Maritime Alps were wetter, while the rest of the Alps were drier (Bartlein et al., 2011; Cheddadi et al., 1996).

As previously mentioned, no proxy-based climate reconstructions from the Maritime Alps extend back to the LGM. The nearest pollen-based reconstructions, which are ≥ 250 km away from our study area, indicate 15–20 ºC colder winter temperatures and ~500 mm/yr lower MAP during the LGM than today (Bartlein et al., 2011; Jost et al., 2005). For the Mediterranean region as a whole, pollen reconstructions indicate that LGM winter temperatures ranged anywhere from 0 to 30 ºC colder than today, while MAP varied between 0 and 800 mm/yr less than today (Wu et al., 2007). Similar to pollen-based reconstructions, numerical ice flow simulations require

183 temperature depressions of at least 10 ºC and at least a 20% reduction in precipitation rates in the
184 southern Alps, including the Maritime Alps, to reproduce the LGM ice extent over the entire
185 Alpine region (Becker et al., 2016). Other reconstructions, however, suggest higher precipitation
186 rates in the Alps during the LGM. Kuhlemann et al. (2008) suggested that incursions of cold
187 polar air between the Pyrenees and the Alps were more frequent during the LGM in order to
188 explain spatial patterns of Mediterranean sea surface temperatures (SSTs) and equilibrium line
189 altitude (ELA) depressions. Such cold air incursions would have resulted in greater moist air
190 convection and cyclogenesis as these air masses encountered the warm SSTs in the Gulf of
191 Genoa and therefore greater precipitation in the Maritime Alps and other Mediterranean-
192 proximal glaciated areas (e.g., Corsica). Higher Alpine precipitation rates during the LGM have
193 also been suggested to result from the southerly deflection of the North Atlantic jet stream in the
194 presence of the North American Ice Sheet (Monegato et al., 2017). This change in circulation
195 would cause greater moisture advection from the Mediterranean Sea northward, as documented
196 by speleothem oxygen isotope records from the northern Swiss Alps (Luetscher et al., 2015),
197 and may explain the delay in maximum ice extent for European Ice Sheet relative to the Alps
198 (Monegato et al., 2017).
199
200 **METHODS**
201 Of the Gesso Valley boulders for which ^{10}Be measurements exist, we obtained archived material
202 (either whole rock or crushed, sieved fractions) from five samples for cosmogenic ^{3}He
203 measurements: one from the Piano del Praiet moraine (PDP10), two from the Ponte Murato
204 moraine (PM1, and PM4), and two from the Tetti del Bandito moraine (TDB1 and TDB3; Fig. 1
205 and Table 1). The ^{10}Be concentration in quartz for PDP10 ($223.8 \pm 9.6 \times 10^{3}$ atoms/g, using the

206 $^{10}Be/^{9}Be$ of Nishiizumi et al. (2007) for NIST SRM4325) was measured at the Scottish
207 Universities Environmental Research Centre Cosmogenic Isotope Analysis Facility in 2013; all
208 other ^{10}Be concentrations are previously published (Federici et al., 2012, 2008). The ^{10}Be
209 exposure ages of these boulders and other boulders from the same moraines have been used to
210 associate the Piano del Praiet, Ponte Murato, and Tetti del Bandito moraines with the Younger
211 Dryas cold period, an intermediate cold period referred to locally as the Bühl stadial at ~18 ka,
212 and the LGM respectively (Federici et al., 2012, 2008). We separated quartz from other phases
213 using standard crushing, sieving, and magnetic methods, followed by a 'frothing' technique
214 commonly used in the ceramics industry to separate quartz from feldspars in the largest sieve
215 fraction that lacked composite grains (Buckenham and Rogers, 1954). Purified quartz was then
216 used to both measure cosmogenic ^{3}He abundances and determine sample-specific ^{3}He diffusion
217 kinetics. All helium isotope measurements were made with an MAP 215-50 sector field mass
218 spectrometer in the BGC Noble Gas Thermochronometry Lab. Gas purification techniques and
219 mass spectrometer analyses are as described in Tremblay et al. (2014b).
220
221 For cosmogenic ^{3}He measurements, 100–500 mg aliquots of quartz were weighed and packed
222 into tantalum metal cups with both ends crimped, placed under vacuum in a sample chamber,
223 and heated with a feedback-controlled 150 W diode laser to either 500, 800, or 1100 ºC for 15
224 minutes until subsequent extractions yielded He signals indistinguishable from the instrumental
225 detection limit. Empty tantalum cup blanks, heated to the same temperatures as the samples, and
226 room temperature procedural blanks were measured throughout each analytical session and
227 subtracted from the sample measurements; ^{3}He blank corrections were typically 2–3 x 10^{4} atoms.
228 Aliquots of air and ^{3}He-spiked helium standards of different manometrically-calibrated pipette

229 volumes were analyzed throughout an instrumental tuning period and used to determine helium
230 sensitivities; sensitivities varied linearly over the pressure range of the sample analyses,
231 estimated by the size of the ^{4}He signal. We propagated uncertainties from the blank corrections
232 and sensitivity regression into the cosmogenic ^{3}He concentrations. We assume that all ^{3}He is
233 cosmogenic.
234
235 To determine sample-specific diffusion kinetics, we conducted stepwise degassing experiments
236 on a proton-irradiated quartz grain from each sample. Proton irradiation generates a uniform
237 distribution of ^{3}He in quartz through similar nuclear reactions to those induced by cosmic ray
238 particles but with ten orders of magnitude or higher production rates, enabling step degassing
239 diffusion experiments to be conducted on single irradiated quartz grains (Shuster et al., 2004;
240 Shuster and Farley, 2005; Tremblay et al., 2014b). We conduct experiments on single grains
241 rather than multi-grain aliquots because it allows us to rapidly achieve and then maintain a
242 spatially homogeneous set point temperature, a critical requirement for step degassing
243 experiments. Previous work (Tremblay et al., 2014b) demonstrates that these single grain
244 experiments are reproducible for different quartz grains from the same sample. Quartz aliquots
245 were irradiated with a 228.5 MeV proton beam for 6 hours at the Francis H. Burr Proton Therapy
246 Center at the Massachusetts General Hospital in December 2015; the total proton fluence for this
247 irradiation was 9.14 x 10^{15} p/cm^{2}. The irradiation target design and setup are detailed in
248 Tremblay et al. (2017). Proton irradiated quartz aliquots were examined with a binocular
249 microscope, and single crystals lacking visible penetrative fractures and inclusions (fluid or
250 mineral) were selected for stepwise degassing. The dimensions of the chosen grains were
251 measured to estimate the spherical equivalent radius used in later calculations to scale the

252 diffusion lengthscale. Details of the stepwise degassing setup and helium measurements are
253 detailed in Tremblay et al. (2014b).
254
255 In addition to determining the spherical equivalent radius of the quartz grains used in diffusion
256 experiments, we also determined the spherical equivalent radii of the quartz grains used for
257 cosmogenic measurements and assessed whether these radii are representative of the quartz size
258 distribution in whole rock. Such an assessment is important because if we significantly reduced
259 the grain size of quartz during the crushing process, this could lead to both an underestimation of
260 the diffusion lengthscale to which the diffusion experiment size is scaled and missing
261 cosmogenic ^{3}He from our measurements. First, we photographed and measured the dimensions
262 of at least 100 quartz grains from the sieve fraction of each sample used for cosmogenic ^{3}He
263 measurements. We determined major, intermediate, and minor axes of best fitting ellipsoids
264 using the software ImageJ (Abràmoff et al., 2004) and calculated the radius of a sphere with the
265 same surface area to volume ratio for each grain. We compared the spherical equivalent radii
266 calculated using this approach to spherical equivalent radii determined from micro x-ray
267 computed tomography (CT) analyses on a smaller number of grains from the same samples,
268 wherein the grains were mapped in three dimensions with a resolution better than 5 micrometers.
269 CT scans were obtained on the Xradia MicroXCT scanner at the University of Texas at Austin
270 High-Resolution X-ray CT Facility and processed using the software Blob3D (Ketcham, 2005)
271 as described in Tremblay et al. (2017). This comparison demonstrates that the ellipsoid approach
272 consistently overestimates the spherical equivalent radius by ~50%, likely because the ellipsoid
273 method significantly underestimates the surface area of grains. We therefore scaled the spherical
274 equivalent radii from loose grain measurements by a factor 1.5; the distribution of grain sizes

from these measurements are shown in Fig. 2. Also shown in Fig. 2 is the probability distribution of spherical equivalent radii of quartz grains in whole rock. To determine this distribution, we determined circular equivalent radii from measured sectional areas of at least 100 quartz grains in thin sections, and inverted the distribution of circular equivalent radii to a distribution of spherical equivalent radii using the code STRIPSTAR and the methodology described by Heilbronner and Barrett (2013). For PDP10, the thin section was made from the same sample as the sample crushed for cosmogenic ^{3}He measurements. For the PM and TDB moraines, no whole rock material from the original samples was preserved; we therefore collected additional material from boulders exposed atop each of these moraines for thin sections, and assume that the grain size observed in these samples is representative of the samples for which we have cosmogenic ^{3}He data.

For all samples, the distribution of spherical equivalent radii for the sieve fraction has a smaller standard deviation than the radii determined from thin section measurements (Fig. 2), which is not surprising given that the sieving process removes larger and smaller grains. With the exception of the PM samples, we find that the mean spherical equivalent radius of quartz in the sieve fraction is equal to or slightly greater than the mean radius determined from thin section measurements (Fig. 2). The mean quartz radius in the sieve fraction from the PM samples is only slightly smaller than the mean radius from thin section measurements, and the two distributions show significant overlap. Given the good agreement between mean spherical equivalent radii for the sieve fraction and thin section quartz, we assume that the grain size has not been substantially reduced by sample crushing and use the mean and standard deviation of the sieve fraction radii distributions as the appropriate diffusion lengthscale for modeling the diffusion of cosmogenic

298 ^{3}He in each sample.

299

300 **RESULTS**

301 We report measured abundances of cosmogenic ^{3}He in quartz aliquots from each of the Gesso
302 Valley samples in Table 2. We used version 3 (v3) of the online exposure age calculator code, a
303 more recent version of the code published in Balco et al. (2008) that implements the cosmogenic
304 ^{3}He production rate in quartz determined by Vermeesch et al. (2009), to calculate an apparent
305 exposure age from the measured ^{3}He abundance in each aliquot. We assume that the erosion rate
306 is negligible for all boulders sampled, as was assumed in the original publications reporting ^{10}Be
307 exposure ages from these boulders (Federici et al., 2012, 2008). Sample coordinates, elevations,
308 thicknesses, and shielding correction factors used in exposure age calculations are reported in
309 Table 1. In Table 3, we report the weighted mean apparent ^{3}He exposure age for each sample
310 determined using the scaling scheme of Stone (2000). We also recalculated the ^{10}Be exposure
311 ages, normalizing the ^{10}Be concentrations to the isotope ratio standards of Nishiizumi et al.
312 (2007), using v3 of the online exposure calculator with version 1.1 of the muogenic production
313 rate code and the CRONUS-Earth primary calibration data set for ^{10}Be production rate (Borchers
314 et al., 2016), and assuming the scaling scheme of Stone (2000) (Table 3). Because the production
315 rates of ^{3}He and ^{10}Be in quartz are not determined from the same calibration datasets, we use the
316 external uncertainties in exposure ages in all calculations that follow. We divided the weighted
317 mean apparent ^{3}He exposure ages by the ^{10}Be exposure ages (both with external uncertainties) to
318 calculate ^{3}He retention, which represents the fraction of cosmogenic ^{3}He produced during
319 surface exposure that remains in the quartz analyzed (Tremblay et al., 2014a).

320

Fig. 3 shows ^{3}He retention as a function of exposure duration in the five samples we analyzed. All Gesso Valley samples retain less than 50% of the cosmogenic ^{3}He that was produced during their exposure (Table 3, Fig. 3). Retention generally decreases with increasing exposure duration: quartz from PDP10, sampled from the highest elevation moraine with an exposure age of 14071 ± 1220 years, retains 46% of its cosmogenic ^{3}He, while quartz from TDB1, sampled from the lowest elevation moraine with an exposure age of 23397 ± 2072 years, retains only 6% of its cosmogenic ^{3}He. Samples PM1 and PM4, both from the Ponte Murato moraine, have similar ^{10}Be exposure ages (16356 ± 1601 years and 19213 ± 1654 years, respectively) but significantly different ^{3}He retention (0.28 ± 0.04 versus 0.36 ± 0.04, respectively; Table 3, Fig. 3). Similarly, the ^{10}Be exposure ages for the two Tetti del Bandito moraine samples, TDB1 and TDB3, are similar (23397 ± 2072 years and 21003 ± 1854 years, respectively), but the ^{3}He retentions in these two samples are drastically different (0.06 ± 0.01 versus 0.29 ± 0.04, respectively; Table 3, Fig. 3).

In order to (1) calculate effective diffusion temperatures (EDTs) and infer temperature histories from the observed ^{3}He retention in quartz from each sample, and (2) assess the differences in ^{3}He retention between samples from the same moraine, we need to know the diffusion kinetics of ^{3}He in each sample. Fig. 4 shows the results of step degassing experiments on proton-irradiated quartz from the Gesso Valley samples in Arrhenius plots where the natural log of diffusivity, calculated from the cumulative fraction of gas released during each heating step (Fechtig and Kalbitzer, 1966), is plotted as a function of inverse temperature (gray circles).

All Gesso Valley quartz samples exhibit some degree of nonlinearity in the Arrhenius plots (Fig.

4). While we do not have a mechanistic explanation or model for this type of complex diffusion behavior (Tremblay et al., 2014b), multiple diffusion domain (MDD) models (Harrison et al., 1991; Lovera et al., 1991; Lovera and Richter, 1989) can reproduce the nonlinearity observed in laboratory degassing experiments and appear to be relevant to ^{3}He diffusive loss over 10^3–10^4 year timescales, as demonstrated for a geologic case study for which the temperatures during surface exposure are reasonably well known (Tremblay et al., 2014b). We constructed MDD models optimized to fit each of the helium step degassing experiments on Gesso Valley quartz samples following the approach outlined in Tremblay et al. (2017). Fig. 5 shows the misfit between the calculated diffusivities from MDD models and the experimentally-determined diffusivities as a function of number of diffusion domains, where the misfit statistic was calculated as in Tremblay et al. (2017). The misfit shown for a given number of diffusion domains is the minimum misfit found after searching over a large range of model parameters (activation energy E_a, pre-exponential factor(s) D_0/a^2, and gas fraction(s)).

We found that, for all five step degassing experiments, increasing the number of diffusion domains from 1 to 2 and from 2 to 3 significantly reduced the misfit between the observed diffusivities and those calculated with the MDD model (Fig. 5). However, increasing the number of diffusion domains from 3 to 4 did not significantly reduce the misfit between the observed and calculated diffusivities (Fig. 5). For experiment PM1-A, attempts at constructing a four domain model yielded two domains with the same pre-exponential factor and thus are the equivalent of the three domain model. Therefore for all experiments we use the diffusion parameters corresponding to the optimized three domain model. Lines corresponding to the diffusion parameters of the three domains, as well as the calculated diffusivities for the three domain

367 models, are shown in color over the experimentally determined diffusivities in Fig. 4. The
368 activation energies, pre-exponential factors, gas fractions, and misfit statistic for these three
369 domain models are reported in Table 4.
370
371 As discussed in Section 2, we need to scale the diffusion kinetics determined from the step
372 degassing experiments to the diffusion lengthscale appropriate for the cosmogenic ^{3}He
373 abundance measurements. In constructing MDD models, we cannot independently parameterize
374 the diffusivity at infinite temperature, D_0, and the diffusion lengthscale, a. Instead, we model
375 them together as the natural logarithm of the pre-exponential factor in the Arrhenius expression,
376 $ln(D_0/a^2)$, which in an Arrhenius plot corresponds to the y-intercept. Because we cannot
377 independently model the diffusion lengthscale a, we must make an assumption about how to
378 scale the MDD models appropriately. This is not a problem for the ^{40}Ar/^{39}Ar thermochronometry
379 community in which MDD models were developed, because in almost all cases argon diffusion
380 kinetics and naturally-occurring argon isotope abundances are measured in the same mineral
381 grain (e.g. Lovera et al., 1997/8). Here, we assume that the diffusion lengthscale of all domains,
382 and by inference all the pre-exponential factors in a given MDD model, scales with the spherical
383 equivalent radius of the quartz grain analyzed. Theoretically, this implies that diffusion
384 lengthscale of the most retentive domain (the domain with the lowest $ln(D_0/a^2)$ or intercept in
385 Arrhenius space) is the spherical equivalent radius of the grain analyzed. Practically, this scaling
386 is accomplished as follows:
387
388 $$\left(\frac{D_0}{a^2}\right)_{scaled} = \left(\frac{D_0}{a^2}\right)_{MDD} \left(\frac{a^2_{sde}}{a^2_{cosmo}}\right) \quad \textbf{(1)}$$
389

where a_{sde} is the spherical equivalent radius of the step degassing experiment quartz grain and a_{cosmo} is the spherical equivalent radius of the quartz grains used for the cosmogenic ^{3}He measurements (Fig. 2).

With the scaled, sample-specific diffusion kinetics, we explore possible temperature scenarios to explain the observed cosmogenic ^{3}He abundances in the Gesso Valley samples. To do this, we use forward models of simultaneous production and diffusion to model how cosmogenic ^{3}He retention evolves as a function of exposure duration under different temperature scenarios. We begin with the simplest possible scenario of constant temperature over time. Although constant temperatures are not climatologically realistic, this calculation allows us to determine the EDT, which is the temperature corresponding to the mean diffusivity for a given temperature history, that is consistent with the observed cosmogenic ^{3}He retention of each sample. These EDTs are equal to or greater than the true mean temperatures the samples experienced over their exposure durations because of the nonlinear relationship between diffusivity and temperature (Tremblay et al., 2014a). Fig. 6 shows the evolution of ^{3}He retention as a function of exposure duration for constant temperature scenarios in 2 ºC increments from 0 ºC to 30 ºC. These retention evolution curves differ for each Gesso Valley quartz sample for several reasons: (1) each sample has a different set of diffusion kinetics, assuming a three domain diffusion model (Fig. 4, Table 4), (2) these sample specific diffusion kinetics are scaled to different spherical equivalent radii based on the measured grain size distributions of quartz in the sieve fraction used for cosmogenic ^{3}He measurements (Fig. 2), and (3) the cosmogenic ^{3}He production rate in quartz differs between samples. In each panel of Fig. 6 we report the integrated EDT that agrees with the observed cosmogenic ^{3}He retention in each quartz sample. We provide two uncertainty estimates on this

integrated EDT. One σ EDT uncertainties in parentheses account for the uncertainty in ^{3}He retention and exposure duration as determined from ^{10}Be measurements; the second set of uncertainties account for uncertainty in the spherical equivalent radius to which the experimentally-determined diffusion kinetics are scaled, in addition to the uncertainties in ^{3}He retention and exposure duration.

The most readily observable feature of the models in Fig. 6 is that the integrated EDT calculated for each quartz sample is different. This is in part expected because the different moraines represented by these samples are located at different elevations in the Gesso Valley, and thus will experience different temperatures at any point in time due to the atmospheric lapse rate. This may also in part be due to the samples having different exposure durations; for example, a change in temperature between the deposition of the TDB moraine and the PM moraine would only be reflected in the cosmogenic ^{3}He retention and integrated EDT of the TDB moraine samples. Differences in integrated EDT between samples from the same moraine, on the other hand, are unexpected. For PM1 we calculate an integrated EDT of 7.6 ºC, while for PM4 we calculate a much higher integrated EDT of 19.7 ºC. Similarly, for TDB1 we calculate an integrated EDT of 24.5 ºC, while for TDB3 we calculate a much lower integrated EDT of 15.8 ºC. These intra-moraine discrepancies preclude a straightforward inversion for changes in EDT through time in the Gesso Valley from the inter-moraine differences in ^{3}He retention. We explore possible causes for these intra-moraine discrepancies in the discussion section; here, we compare our observations to modern and paleoclimate observations and simulations to assess whether the EDTs we calculate are plausible for the Gesso Valley since the LGM.

436 To contextualize these EDTs integrated over the exposure duration of each sample, in Fig. 7 we
437 use modern daily temperature records from 2002 to 2016 to calculate present-day mean
438 temperatures (solid lines) and EDTs (dashed lines) at the elevation of each moraine. We might
439 expect present-day EDTs at each moraine to be comparable to or greater than the EDT integrated
440 over the samples' exposure durations, considering that mean temperatures during the early, pre-
441 Holocene exposure history of each sample were likely lower than today. However, this
442 expectation may be overly simplistic, as changes in the amplitude of daily and seasonal
443 temperatures since the LGM will also affect the integrated EDTs. Nonetheless, calculation of
444 modern EDTs provides an estimate for the magnitude of the difference between mean
445 temperatures and EDTs due to temperature variations on daily and seasonal timescales in the
446 Gesso Valley.
447
448 We obtained temperature records at the elevation of each moraine by scaling daily mean,
449 minimum, and maximum temperature data from two meteorological stations within the Gesso
450 Valley: Diga della Piastra (44.227 ºE, 7.389 ºN, 959 m) and Diga del Chiotas (44.168 ºE, 7.334
451 ºN, 1980 m). These data are publicly available through the Environmental Protection Agency for
452 the Piemonte Region (arpa.piemonte.gov.it). We scaled the temperature data at Diga della Piastra
453 to the elevation of the TDB and PM moraines and the temperature data at Diga del Chiotas to the
454 elevation of the PDP moraine using monthly average lapse rates determined from the same
455 dataset (minimum = 2.8 ºC/km in December/January; maximum = 6.7 ºC/km in May), and
456 calculated the modern EDT using these scaled temperature data and the activation energies of the
457 best fit MDD models in Fig. 4 and Table 4. The modern EDTs at the three morain elevations are
458 ~4–5 ºC greater than the mean temperatures, reflecting the effect of daily and seasonal

459 temperature amplitudes on the mean diffusivity and EDT. We do not observe a consistent
460 relationship between modern EDT, calculated at the elevation of each moraine, and integrated
461 EDTs calculated for each sample. For PM4 and TDB1, the modern EDT estimate (15.1 and 15.9
462 ºC) is several degrees lower than the EDT integrated over each sample's exposure duration (19.7
463 +3.5/–3.7 and 24.5 +4.3/–3.9 ºC). In contrast, the modern EDT estimates for PDP10 and TDB3
464 (9.8 and 15.9 ºC) are comparable to the EDTs integrated over their exposure durations (13.8
465 +4.3/–5.7 and 15.8 +3.9/–4.5 ºC), and for PM1 the modern EDT estimate (15.0 ºC) is several
466 degrees higher (vs. 7.6 +3.5/–3.4 ºC).
467
468 In addition to comparing the integrated EDTs calculated from observed cosmogenic ^{3}He
469 abundances to modern day EDTs in the Gesso Valley, we can compare our cosmogenic ^{3}He
470 observations to the those that would result from (1) temperature histories simulated in general
471 circulation models (GCMs), and (2) temperature reconstructions based on other proxies at nearby
472 locations. GCM simulations and independent proxy reconstructions provide more realistic late
473 Quaternary temperature scenarios with which to test the plausibility of our cosmogenic ^{3}He
474 observations. As cosmogenic noble gas paleothermometry is refined and improved, cosmogenic
475 ^{3}He observations will also be useful for assessing the fidelity of these paleoclimate simulations
476 and reconstructions based on other proxies. For both model and proxy comparisons, the
477 temperature history used to model cosmogenic ^{3}He abundances must be equal in duration to the
478 moraine sample exposure.
479
480 Most GCM paleo-experiments simulate climate at a particular point in time, such as the mid-
481 Holocene or LGM; only a handful of GCMs simulations have explored transient climate

evolution in the Holocene and latest Pleistocene. Here, we model how cosmogenic ^{3}He retention would evolve as a function of exposure duration using seasonal temperature outputs from the TraCE-21ka transient simulation. TraCE-21ka uses the National Center for Atmospheric Research (NCAR) Community Climate System Model version 3 (CCSM3), a synchronously coupled atmosphere-ocean general circulation model (GCM) (Collins et al., 2006), to simulate the Earth's climate from the LGM (22 thousand years ago) to the present (He, 2011; Liu et al., 2009). We obtained mean and maximum seasonal (DJF, MAM, JJA, and SON) temperatures from the TraCE-21ka simulation for the 44.3 ºN, 7.4 ºE grid cell including the Gesso Valley. We chose mean and maximum seasonal temperatures for practical reasons (sub-seasonal temporal resolution is computationally unwieldy), but also because these represent endmember EDT scenarios for the moraines in Gesso Valley. Mean seasonal temperatures represent the low-EDT endmember, as this scenario implies that the mean temperatures represent the full amplitude of seasonal temperature variation and that there is no sub-seasonal (e.g., daily) variability. Maximum seasonal temperatures represent the high-EDT endmember, as this scenario implies that the maximum sub-seasonal temperature simulated during a three month interval is the temperature over the duration of that season. We thus expect the observed cosmogenic ^{3}He retention in our samples to be bracketed by the predicted cosmogenic ^{3}He retention from these endmember scenarios, with the mean seasonal temperature scenario placing an upper bound on cosmogenic ^{3}He retention and the maximum seasonal temperature placing a lower bound.

TraCE-21ka simulation temperatures were determined for a mean elevation above sea level for the grid cell, which changed through the simulation as simulated sea level changed. However, the elevation of our sample sites with respect to sea level would have also changed through time,

meaning that the relative offset between our sample site elevation and the mean grid cell elevation would have remained constant. We therefore scale the TraCE-21ka simulation temperatures to our sample sites using the present day difference between the sample site elevations and TraCE-21ka mean elevation assuming the modern seasonal lapse rate determined from the meteorological stations discussed above. The atmospheric lapse rate in the Gesso Valley likely changed between the LGM and the present, especially considering the fact that the valley was more extensively glaciated during part of this interval. Nonetheless, we assume the modern rate because (1) we have no independent means for assessing how different paleo-lapse rates may have been, and (2) any differences from the modern lapse rate when the valley was glaciated were likely ≤ 2 ºC/km (e.g. Davis et al., 2003; Gardner et al., 2009; Loomis et al., 2017), which will not be resolvable using our cosmogenic noble gas observations that span ≤ 1 km in elevation (Tremblay et al., 2014a).

For all Gesso Valley quartz samples, the observed cosmogenic ^{3}He retention is bracketed by the ^{3}He retention calculated assuming mean seasonal temperatures and the ^{3}He retention calculated assuming maximum seasonal temperatures scaled from the TraCE-21ka simulation. For PDP10 (Fig. 8), PM4 (Fig. 9), and TDB1 (Fig. 10), we calculate cosmogenic ^{3}He retention from the TraCE-21ka simulation maximum seasonal temperature that is in agreement within uncertainty with the observed retention in these samples. Cosmogenic ^{3}He retention calculated from the TraCE-21ka mean seasonal temperatures agrees with the observed cosmogenic ^{3}He retention in PM1 within uncertainty (Fig. 9), while for TDB3 the observed cosmogenic ^{3}He retention lies between that predicted from the mean and maximum seasonal TraCE-21ka temperatures.

528 We also use chironomid-based July temperature reconstructions from other Alpine locations to
529 model cosmogenic ^{3}He retention for comparison with our cosmogenic ^{3}He observations. Like the
530 maximum seasonal temperatures from the TraCE-21ka simulation, the mean July temperature
531 inferred from chironomids is a high-EDT endmember scenario, as this scenario implies that the
532 mean July temperature is representative of sub-annual temperatures. The lack of Alpine
533 chironomid records before 16 cal. years BP prevents us from using chironomid-based July
534 temperature reconstructions to model cosmogenic ^{3}He retention in PM4, TDB1, and TDB3.
535 However, we can splice together chironomid records from several locations to obtain coeval
536 coverage with samples PDP10 and PM1, which have the youngest ^{10}Be exposure ages of 14071
537 ± 1220 and 16356 ± 1601 years, respectively.
538
539 The most proximal chironomid-based mean July temperature reconstruction is from Lago
540 Piccolo di Avigliana (LPA), located in the Italian Alps ~80 km north of the Gesso Valley (45.05
541 ºN; 7.38 ºE, 365 m), where the record extends from 14200 to 9500 cal. year BP (Larocque and
542 Finsinger, 2008). In order to obtain coeval coverage with the exposure ages of PDP10 and PM1,
543 we spliced the LPA record with chironomid July temperature reconstructions from: Schwarzsee
544 ob Sölden (SOS), a high-alpine lake in the Austrian Alps (46.96583 ºN, 10.94611 ºE, 2796 m)
545 with a chironomid record from 10200 to –36 cal. years BP (Ilyashuk et al., 2011); Lac Lautrey
546 (LAU), a small lake in the French Jura Mountains (46.58722 ºN, 5.86389 ºE, 788 m) with a
547 chironomid record from 15908 to 11033 cal. years BP (Heiri and Millet, 2005); and
548 Hinterburgsee (HIN), a subalpine lake in the northern Swiss Alps (46.71833 ºN, 8.06750 ºE,
549 1515 m) with a chironomid record from from 12210 to 1900 cal. years BP (Heiri et al., 2004).
550 Like the GCM simulation, we scaled the July temperature reconstructions from each location to

551 the elevations of PDP10 and PM1 using modern lapse rate information, and when temporal
552 overlap occurred between two or more chironomid records we used an average of the scaled
553 temperatures weighted by the inverse distance between the chironomid sites and our study site.
554
555 In Figs. 8 and 9 we show the scaled, spliced July temperature reconstruction using all four
556 chironomid records and the corresponding model for cosmogenic ^{3}He retention in PDP10 and
557 PM1, respectively. We found that different chironomid record splices (e.g., SOS + LPA; SOS +
558 HIN + LPA; SOS + LPA + LAU; SOS + HIN + LPA +LAU) result in very small differences in
559 modeled cosmogenic ^{3}He retention; therefore only the four record splice (SOS + HIN + LPA
560 +LAU) is shown. Like the maximum seasonal temperatures from the TraCE-21ka simulation, we
561 model cosmogenic ^{3}He retention from the mean July temperature reconstruction that agrees with
562 our observations from PDP10 and that underestimates the observed ^{3}He retention in PM1.
563
564 **DISCUSSION**
565 To a first order, the fact that cosmogenic ^{3}He retention calculated with endmember temperature
566 scenarios from a GCM simulation and an independent proxy reconstruction brackets our
567 cosmogenic ^{3}He observations indicates that the ^{3}He observations record ambient temperatures
568 with some accuracy. The observation that our integrated EDTs are not tens of degrees different
569 from modern EDTs in the Gesso Valley calculated with meteorological data also indicates
570 accuracy, as temperature differences between the present-day and LGM were unlikely to exceed
571 15 ºC (e.g., Becker et al., 2016), and post-LGM temperature differences were likely to be much
572 smaller. This first order agreement suggests that our cosmogenic ^{3}He measurements are
573 providing meaningful information on ambient temperature conditions during exposure. For

574 example, we do not calculate integrated EDTs below 0 ºC, as we do for cosmogenic ^{3}He
575 measurements made on Holocene-age glacial erratics in Antarctica (Tremblay et al., 2014a), nor
576 do we calculate integrated EDTs unfeasibly high for Earth surface conditions (e.g, EDTs of 70–
577 80 ºC that we obtain for the Moon (Shuster and Cassata, 2015)). However, for the purposes of
578 reconstructing past climate variations, the substantial intra-moraine differences in EDTs are
579 problematic, precluding us from carrying out a straightforward inversion for changes in EDT
580 through time in the Gesso Valley from the inter-moraine differences in ^{3}He retention. For both
581 the PM and TDB moraines, the difference in integrated EDTs between samples from the same
582 moraine is ~10 ºC. These intra-moraine differences require explanation.
583
584 One possibility is that these intra-moraine temperature differences are real and reflect differential
585 shading of the samples by vegetation, snow cover or topography. For example, patchy vegetation
586 on a moraine crest may cause one boulder to be fully shaded under a tree canopy, while another
587 boulder tens of meters away remains unshaded. Similarly, boulders nearby to one another might
588 accumulate substantial or insignificant snow cover depending on their relative positioning and
589 shielding from prevailing winds during the wintertime. Unshaded rock samples can experience
590 significantly higher daytime temperatures due to insolation than shaded samples. As discussed in
591 Tremblay et al. (2014a), heating of rocks due to incident solar radiation can substantially raise
592 rock temperatures above daily maximum air temperatures. Amplification of temperatures 5–10
593 ºC above the daily maximum is common in non-desert environments (Bartlett et al., 2006; Hall et
594 al., 2005; McGreevy, 1985; Schwarz et al., 2012). Considering our modern EDT calculations
595 from meteorological station data, if we increase the maximum daily temperature by 5 or 10 ºC,
596 we find significant increases in the EDT. For example, using the diffusion kinetics for TDB1, by

increasing the maximum daily temperature in the meteorological data by 5 ºC, we find that EDT increases from 15.9 to 19.2 ºC. Increasing the maximum daily temperature by 10 ºC increases the EDT to 23.0 ºC, which is within the uncertainty of the EDT integrated over TDB1's exposure duration. Therefore it is possible that, in the case of the TDB moraine, TDB3 may have been shaded or snow covered during all or some of its exposure history, while TDB1 was fully exposed to incoming solar radiation throughout its exposure. Similarly, PM1 may have been shaded or snow covered while PM4 was not since the PM moraine was deposited.

This interpretation is consistent with the comparison of observed cosmogenic ^{3}He retention to calculated retention from TraCE-21ka and chironomid temperatures. Observations from PDP10, PM4, and TDB1 are closest to the TraCE-21ka simulation maximum seasonal temperature calculations, while observations from PM1 are closer to the calculations with the mean seasonal temperature and observations from TDB3 lie between the predicted ^{3}He retention from mean and maximum seasonal temperature scenarios. We would expect mean temperatures to agree with our cosmogenic ^{3}He observations, as is the case for PM1, if no heating due to insolation occurred. Following the same reasoning, we anticipate that samples experiencing nonzero insolation will have cosmogenic ^{3}He abundances that are lower than what is expected from mean air temperatures, as is the case for PDP10, PM4, TDB1, and TDB3. Likewise, the apparent agreement between the observed cosmogenic ^{3}He retention in PDP10 and the chironomid-based reconstruction of mean July temperatures, which will be significantly greater than mean temperatures throughout most of the year, supports the interpretation that the temperatures experienced by sample PDP10 exceeded air temperatures during its exposure to cosmic ray particles. A more precise relationship between insolation-induced daily rock temperature

620 amplifications and maximum seasonal air temperatures or mean July air temperatures could be
621 obtained by monitoring *in situ* rock temperatures adjacent to meteorological stations, such that
622 these temperature scenarios are could be adjusted and provide more information than just a high-
623 EDT endmember.
624
625 We note that shading from solar radiation and shielding of cosmic rays are not equivalent.
626 Vegetative cover can have a substantial effect on heating by insolation, but in most cases a
627 negligible effect on cosmogenic nuclide production rates due to its relatively low density.
628 Similarly, thin snow cover will not substantially affect cosmogenic nuclide production rates but
629 will cause rock temperatures to differ substantially from air temperatures. Thick snow cover (≥ 1
630 m) will affect both production rates and temperatures. Today, there is significant vegetation
631 cover on the TDB and PM moraines, but no cover at PDP. Unfortunately, we have no way of
632 assessing the degree of vegetation cover on the TDB and PM moraines before the modern era,
633 and no way to assess the past degree of snow cover for all moraines (although observations of in
634 situ 14C in quartz could help address snow cover; e.g., Hippe et al., 2014). Topography can
635 shield rocks from cosmic ray particles, but these effects are accounted for in our calculations of
636 cosmogenic nuclide production rates (Table 1); in contrast, we have not accounted for the effects
637 of topographic shading on rock surface temperatures. We do not have detailed enough locations
638 for the TDB and PM samples to identify the original boulders that were sampled and assess
639 differences in topographic shading, although we suspect this would be secondary to vegetation
640 and snow cover effects.
641
642 Another possible explanation for the intra-moraine differences is that our MDD model

643 representations of helium diffusion kinetics in Gesso Valley quartz samples are inaccurate and/or
644 inadequate. The MDD models we construct are inherently non-unique, and while the models we
645 use minimize the misfit between the observed and calculated diffusivities in our step degassing
646 experiments for a given number of domains, comparable fits can be achieved over a range of
647 diffusion parameters. To illustrate this, in Fig. 11 we show minimized values of MDD model
648 misfit, calculated using the misfit statistic defined in Tremblay et al. (2017), as a function of
649 activation energy E_a for three domain models fit to each of the step degassing experiments
650 shown in Fig. 4. For most of the step degassing experiments, there is a broad range of activation
651 energies (and associated pre-exponential factors and gas release fractions) over which the misfit
652 with the MDD model changes only slightly; these changes in misfit are much smaller than the
653 change in misfit associated with increasing the number of diffusion domains and the model
654 complexity (Fig. 5).
655
656 For example, the MDD misfit for the PM1-A step degassing experiment ranges between 7.0 and
657 10.2% between activation energies of 80 and 97.5 *kJ/mol* (Fig. 11). The MDD diffusion kinetics
658 we use in the forward models for PM1 quartz presented above assume an activation energy of
659 89.6 *kJ/mol*. If instead we use a different set of diffusion kinetics for a three domain model that
660 yields a comparable misfit with the step degassing experiment (E_a = 97.5 *kJ/mol*; $ln(D_0/a^2)$ =
661 12.2, 10.1, 16.8; f_{gas} = 0.45, 0.44, 0.11; Misfit = 0.095), we calculate an integrated EDT from the
662 cosmogenic ^{3}He retention in PM1 quartz of 17.8 (± 2.3) +3.8/-3.9 ºC, which is in agreement with
663 the integrated EDT we calculated for PM4 (Fig. 6). This highlights how sensitive the
664 temperatures we calculate from an observed amount of cosmogenic ^{3}He retention are to the
665 diffusion kinetics we use. While different MDD models might reproduce diffusivities observed

666 in laboratory step degassing experiments comparably well, the downward extrapolation of these
667 models results in significantly different diffusivities at the temperatures characterizing Earth's
668 surface. This suggests that some or all of the intra-moraine differences in integrated EDTs could
669 be attributed to uncertainties in how we extrapolate laboratory-determined diffusion kinetics.
670 Given that we do not yet have a mechanistic understanding of what controls the complex noble
671 gas diffusion behavior we observe in our experiments, discriminating between different MDD
672 models of comparably good fit (and even assessing whether MDD models adequately represent
673 the processes responsible for complex behavior) is difficult at this stage.
674
675 A third possible explanation for the intra-moraine variation could arise from our grain size
676 analysis and scaling of MDD models. Uncertainty in the physical significance of our MDD
677 models translates into an uncertainty in our assumptions about how to scale our MDD model fits
678 from step degassing experiments to the cosmogenic ^{3}He measurements. However, because we
679 have scaled the results of each experiment using the same assumptions in Eq. 1, the effects will
680 be systematic. Similarly, the factor of 1.5 we applied to estimated spherical equivalent radii of
681 quartz from the sieve fractions, based on different approaches to estimate surface area to volume
682 ratios and ground truthing with x-ray computed tomography data, will have systematic effects on
683 all integrated EDTs. Assuming that the MDD model scaling and correction applied to sieve
684 fraction measurements are appropriate, we must also consider the possibility that our grain size
685 analysis for the PM and TDB samples does not represent the actual grain size and diffusion
686 lengthscale of quartz in these samples. Since we did not have whole rock material from the
687 original PM and TDB samples, we made thin sections from other boulders collected from the PM
688 and TDB moraines to compare with the size distributions of quartz in the sieved fraction. While

689 there is good agreement between the mean spherical equivalent radii of quartz measured in these
690 thin sections and in the sieve fractions, it is possible that in the original sample the mean quartz
691 size before crushing was much larger. As a sensitivity test, we again use PM1 as an example. In
692 order to obtain an integrated EDT for PM1 equivalent to that calculated for PM4 of 19.7 ºC, we
693 must increase the spherical equivalent radius assumed for the cosmogenic ^{3}He measurement by
694 110% (without changing the spherical equivalent radius for PM4). While such a dramatic
695 underestimation of the PM1 grain size, and more generally >100% uncertainty in all our PM and
696 TDB grain size analyses, seems unlikely, we cannot rule out such a possibility given that whole
697 rock material from these samples was unavailable.
698
699 As a final potential source of intra-moraine variation, the moraine boulders that we sampled may
700 have more complex exposure histories than we allow for in our production and diffusion models,
701 either due to cosmogenic ^{10}Be and ^{3}He inheritance or due to nonzero erosion rates that vary
702 between boulders. More complex exposure histories are plausible for all three moraines, as the
703 ^{10}Be exposure ages from a given moraine do not entirely overlap within their internal
704 uncertainties (Table 3). Although we only studied one boulder from the PDP moraine,
705 cosmogenic ^{10}Be measurements for four additional PDP boulders also exhibit dispersion that
706 cannot be explained by measurement uncertainty alone (Federici et al., 2008). PDP10, the
707 sample studied here, has the oldest exposure age of the five boulders with ^{10}Be measurements.
708 We do not have measurements of additional cosmogenic nuclides (e.g., ^{26}Al, *in situ* ^{14}C) to test
709 whether our samples exhibit evidence for complex exposure. Nonetheless, we can explore what
710 effects inheritance and nonzero erosion might have on our cosmogenic ^{3}He observations and the
711 EDTs we calculate from them.

712

713 Inheritance would most likely affect the boulders from each moraine with the oldest apparent
714 ^{10}Be exposure ages: PDP10, PM4, and TDB1. The cosmogenic ^{3}He observations from these
715 boulders yield higher integrated EDTs than other boulders from the same moraine (in the case of
716 PM4 and TDB1) and are closest to the ^{3}He retention calculated using the high-EDT endmember
717 scenarios (maximum seasonal temperatures from TraCE-21ka and mean July temperatures from
718 spliced chironomid records). In order for inheritance to explain these observations and the intra-
719 moraine differences in integrated EDT, the quartz in these boulders would have to lose a
720 substantial proportion of their inherited ^{3}He relative to inherited ^{10}Be. This is not unreasonable
721 considering that temperature-dependent diffusive loss would also affect cosmogenic ^{3}He
722 produced prior to boulders being deposited in a moraine; thus we consider inheritance to be a
723 viable option to explain some of the intra-moraine discrepancies we observe.

724

725 In contrast, nonzero erosion rates will likely affect the boulders from each moraine with the
726 youngest apparent ^{10}Be exposure ages: PM1 and TDB3. The cosmogenic ^{3}He observations from
727 these boulders yield lower integrated EDTs than other boulders from the same moraine and are
728 closer to the ^{3}He retention calculated using the low-EDT endmember scenario (mean seasonal
729 temperatures from TraCE-21ka). If we assume that 15 cm of material has been eroded since the
730 initial exposures of PM1 and TDB3–corresponding to the depth at which daily temperature
731 oscillations typically become negligible in rock (Tremblay et al., 2014a)–and that the exposure
732 ages calculated from ^{10}Be measurements from PM4 and TDB1 are the respective true exposure
733 ages, we can recalculate the ^{10}Be exposure age, ^{3}He apparent exposure age, and ^{3}He retention for
734 PM1 and TDB3. This results in an increase in ^{10}Be exposure age (e.g., from 16356 ± 1023 to

735 18821 ± 1335 for PM1), but not a substantial decrease in ^{3}He retention (e.g., from 0.28 ± 0.04 to
736 0.25 ± 0.04 for PM1). As a consequence, the integrated EDTs we would calculate for these
737 samples including the effects of erosion would not be substantially higher than those we
738 calculated assuming no erosion. Thus the effects of variable erosion seem unlikely to fully
739 explain the intra-moraine differences we observe.
740
741 In summary, there is substantial intra-moraine variability in the integrated EDTs we calculate
742 from our cosmogenic ^{3}He observations that requires explanation. We have outlined four major
743 sources of uncertainty in our approach that could explain these intra-moraine variations.
744 Ultimately, these potential sources of uncertainty are too under-constrained at this time to allow
745 for a straightforward interpretation about the climate history of the Maritime Alps during
746 deglaciation. Nonetheless, we calculate integrated EDTs for all samples that are bracketed by
747 plausible endmember EDT scenarios for the Gesso Valley based on mean and maximum
748 seasonal temperatures from the TraCE-21ka simulation and on chironomid-derived mean July
749 temperature reconstructions. The trend toward the high-EDT endmember scenarios for all
750 samples except PM1 is not surprising, given that we expect integrated EDTs to exceed the mean
751 ambient temperatures in a sample's exposure history because of the nonlinear dependence of
752 diffusivity on temperature. The observation that our integrated EDTs are not drastically different
753 from modern EDTs in the Gesso Valley is also encouraging, given the magnitude of plausible
754 temperature differences between the LGM and today. Collectively, these results demonstrate
755 promise for the application of cosmogenic noble gas paleothermometry in paleoclimate studies,
756 provided that the four major sources of uncertainty we detail above are accounted for in future
757 applications.

CONCLUSIONS

Integrated EDTs since the LGM in the Gesso Valley, calculated from our observations of cosmogenic ^{3}He concentrations in quartz, range from 8 to 25 ºC and are consistent with what we expect from modern meteorological station data, a GCM simulation of Earth's climate since the LGM, and data from independent proxies in the region. Nonetheless, there are nontrivial differences between the integrated EDTs we calculate, particularly for samples from the same moraine, that require explanation. We identify four major potential sources of uncertainty that could account for these discrepancies: (1) the fact that we have not accounted for variations in radiative heating of the boulder surfaces across samples due to differential shading, (2) limitations in our understanding of and ability to model and extrapolate helium diffusion kinetics when complex behavior is observed, (3) uncertainties associated with our quartz grain size analyses, and (4) unaccounted for erosion or cosmogenic inheritance. At this stage, all four of these possibilities could be contributing to intra-moraine and inter-moraine variability in reconstructed temperatures. Because of these uncertainties, and the fact that we have no cosmogenic ^{3}He observations from younger moraines that record only Holocene temperatures in the Gesso Valley, it is difficult to fully compare our results to the TraCE-21ka and chironomid temperature records, or to invert our results directly for changes in EDT through time in the Gesso Valley from the inter-moraine differences in ^{3}He retention. As a consequence, it is not yet possible to use these data to test the hypothesis that the post-LGM climate evolution and glacier dynamics of the Maritime Alps differed from other Alpine regions with our dataset. These results nonetheless demonstrate first order accuracy in the temperatures constrained by cosmogenic noble gas paleothermometry, and suggest that with additional work and better understanding of

781 diffusion kinetics and rock-air temperature relationships, we can improve the precision of past
782 temperature constraints to address questions in paleoclimate in future applications.
783
784 **ACKNOWLEDGEMENTS**
785 MMT and DLS acknowledge support from the NSF Petrology and Geochemistry Program
786 (EAR-1322086 to DLS), the UC Berkeley Larsen Grant, and the Ann and Gordon Getty
787 Foundation. MMT was supported by an NSF Graduate Research Fellowship. MS acknowledges
788 support from the Royal Society (IE150603), the Leverhulme Trust (IAF-2016-001) and NERC
789 (CIAF 9092.1010).
790
791 **REFERENCES CITED**
792 Abràmoff, M.D., Magalhães, P.J., Ram, S.J., 2004. Image processing with ImageJ. Biophotonics
793 international 11, 36–42.
794 Annan, J.D., Hargreaves, J.C., 2015. A perspective on model-data surface temperature
795 comparison at the Last Glacial Maximum. Quat. Sci. Rev. 107, 1–10.
796 Annan, J.D., Hargreaves, J.C., 2013. A new global reconstruction of temperature changes at the
797 Last Glacial Maximum. Clim. Past 9, 367–376.
798 Balco, G., Stone, J.O., Lifton, N.A., Dunai, T.J., 2008. A complete and easily accessible means
799 of calculating surface exposure ages or erosion rates from ^{10}Be and ^{26}Al measurements.
800 Quat. Geochronol. 3, 174–195.
801 Bartlein, P.J., Harrison, S.P., Brewer, S., Connor, S., Davis, B., Gajewski, K., Guiot, J.,
802 Harrison-Prentice, T.I., Henderson, A., Peyron, O., Others, 2011. Pollen-based continental
803 climate reconstructions at 6 and 21 ka: a global synthesis. Clim. Dyn. 37, 775–802.

804 Bartlett, M.G., Chapman, D.S., Harris, R.N., 2006. A decade of ground--air temperature tracking
805 at Emigrant Pass Observatory, Utah. J. Clim. 19, 3722–3731.
806 Becker, P., Seguinot, J., Jouvet, G., Funk, M., 2016. Last Glacial Maximum precipitation pattern
807 in the Alps inferred from glacier modelling. Geogr. Helv. 71, 173–187.
808 Blaga, C.I., Reichart, G.-J., Lotter, A.F., Anselmetti, F.S., Sinninghe Damsté, J.S., 2013. A TEX
809 86 lake record suggests simultaneous shifts in temperature in Central Europe and Greenland
810 during the last deglaciation : A SWISS TEX 86 LAKE RECORD. Geophys. Res. Lett. 40,
811 948–953.
812 Borchers, B., Marrero, S., Balco, G., Caffee, M., Goehring, B., Lifton, N., Nishiizumi, K.,
813 Phillips, F., Schaefer, J., Stone, J., 2016. Geological calibration of spallation production
814 rates in the CRONUS-Earth project. Quat. Geochronol. 31, 188–198.
815 Brisset, E., Guiter, F., Miramont, C., Revel, M., Anthony, E.J., Delhon, C., Arnaud, F., Malet, E.,
816 de Beaulieu, J.-L., 2015. Lateglacial/Holocene environmental changes in the Mediterranean
817 Alps inferred from lacustrine sediments. Quat. Sci. Rev. 110, 49–71.
818 Buckenham, M.H., Rogers, J., 1954. Flotation of quartz and feldspar by dodecylamine.
819 Transactions of Institute of Mining and Metallurgy 64, l–30.
820 Casazza, G., Grassi, F., Zecca, G., Minuto, L., 2016. Phylogeographic Insights into a Peripheral
821 Refugium: The Importance of Cumulative Effect of Glaciation on the Genetic Structure of
822 Two Endemic Plants. PLoS One 11, e0166983.
823 Cheddadi, R., Bar-Hen, A., 2009. Spatial gradient of temperature and potential vegetation
824 feedback across Europe during the late Quaternary. Clim. Dyn. 32, 371–379.
825 Cheddadi, R., Yu, G., Guiot, J., Harrison, S.P., Prentice, I.C., 1996. The climate of Europe 6000
826 years ago. Clim. Dyn. 13, 1–9.

827 Collins, W.D., Bitz, C.M., Blackmon, M.L., Bonan, G.B., Bretherton, C.S., Carton, J.A., Chang,
828 P., Doney, S.C., Hack, J.J., Henderson, T.B., Others, 2006. The community climate system
829 model version 3 (CCSM3). J. Clim. 19, 2122–2143.
830 Davis, B.A.S., Brewer, S., Stevenson, A.C., Guiot, J., 2003. The temperature of Europe during
831 the Holocene reconstructed from pollen data. Quat. Sci. Rev. 22, 1701–1716.
832 Durand, Y., Giraud, G., Laternser, M., Etchevers, P., Mérindol, L., Lesaffre, B., 2009a.
833 Reanalysis of 47 years of climate in the French Alps (1958–2005): climatology and trends
834 for snow cover. J. Appl. Meteorol. Climatol. 48, 2487–2512.
835 Durand, Y., Laternser, M., Giraud, G., Etchevers, P., Lesaffre, B., Mérindol, L., 2009b.
836 Reanalysis of 44 yr of climate in the French Alps (1958–2002): methodology, model
837 validation, climatology, and trends for air temperature and precipitation. J. Appl. Meteorol.
838 Climatol. 48, 429–449.
839 Fechtig, H., Kalbitzer, S., 1966. The diffusion of argon in potassium-bearing solids, in:
840 Potassium Argon Dating. Springer, pp. 68–107.
841 Federici, P.R., Granger, D.E., Pappalardo, M., Ribolini, A., Spagnolo, M., Cyr, A.J., 2008.
842 Exposure age dating and Equilibrium Line Altitude reconstruction of an Egesen moraine in
843 the Maritime Alps, Italy. Boreas 37, 245–253.
844 Federici, P.R., Granger, D.E., Ribolini, A., Spagnolo, M., Pappalardo, M., Cyr, A.J., 2012. Last
845 Glacial Maximum and the Gschnitz stadial in the Maritime Alps according to ^{10}Be
846 cosmogenic dating. Boreas 41, 277–291.
847 Federici, P.R., Pappalardo, M., Ribolini, A., 2003. Geomorphological map of the Maritime Alps
848 Natural Park and surroundings (Argentera Massif, Italy). 1: 25,000 scale. Selca, Florence.
849 Federici, P.R., Ribolini, A., Spagnolo, M., 2017. Glacial history of the Maritime Alps from the

Last Glacial Maximum to the Little Ice Age. Geological Society, London, Special Publications 433, 137–159.

Gandouin, E., Franquet, E., 2002. Late Glacial and Holocene chironomid assemblages in Lac Long Inférieur (southern France, 2090 m): palaeoenvironmental and palaeoclimatic implications. J. Paleolimnol. 28, 317–328.

Gardner, A.S., Sharp, M.J., Koerner, R.M., Labine, C., Boon, S., Marshall, S.J., Burgess, D.O., Lewis, D., 2009. Near-surface temperature lapse rates over Arctic glaciers and their implications for temperature downscaling. J. Clim. 22, 4281–4298.

Gourbet, L., Shuster, D.L., Balco, G., Cassata, W.S., Renne, P.R., Rood, D., 2012. Neon diffusion kinetics in olivine, pyroxene and feldspar: retentivity of cosmogenic and nucleogenic neon. Geochim. Cosmochim. Acta 86, 21–36.

Granger, D.E., Lifton, N.A., Willenbring, J.K., 2013. A cosmic trip: 25 years of cosmogenic nuclides in geology. Geol. Soc. Am. Bull. 125, 1379–1402.

Hall, K., Lindgren, B.S., Jackson, P., 2005. Rock albedo and monitoring of thermal conditions in respect of weathering: some expected and some unexpected results. Earth Surf. Processes Landforms 30, 801–812.

Harrison, S.P., Bartlein, P.J., Izumi, K., Li, G., Annan, J., Hargreaves, J., Braconnot, P., Kageyama, M., 2015. Evaluation of CMIP5 palaeo-simulations to improve climate projections. Nat. Clim. Chang. 5, nclimate2649.

Harrison, T.M., Lovera, O.M., Matthew, T.H., 1991. $^{40}Ar/^{39}Ar$ results for alkali feldspars containing diffusion domains with differing activation energy. Geochim. Cosmochim. Acta 55, 1435–1448.

He, F., 2011. Simulating transient climate evolution of the last deglaciation with CCSM 3.

873 Heilbronner, R., Barrett, S., 2013. Image analysis in Earth sciences: microstructures and textures
874 of earth materials. Springer Science & Business Media.
875 Heiri, O., Brooks, S.J., Renssen, H., Bedford, A., Hazekamp, M., Ilyashuk, B., Jeffers, E.S.,
876 Lang, B., Kirilova, E., Kuiper, S., Others, 2014. Validation of climate model-inferred
877 regional temperature change for late-glacial Europe. Nat. Commun. 5, 4914.
878 Heiri, O., Millet, L., 2005. Reconstruction of Late Glacial summer temperatures from
879 chironomid assemblages in Lac Lautrey (Jura, France). J. Quat. Sci. 20, 33–44.
880 Heiri, O., Tinner, W., Lotter, A.F., 2004. Evidence for cooler European summers during periods
881 of changing meltwater flux to the North Atlantic. Proc. Natl. Acad. Sci. U. S. A. 101,
882 15285–15288.
883 Hippe, K., Ivy-Ochs, S., Kober, F., Zasadni, J., Wieler, R., Wacker, L., Kubik, P.W., Schlüchter,
884 C., 2014. Chronology of Lateglacial ice flow reorganization and deglaciation in the
885 Gotthard Pass area, Central Swiss Alps, based on cosmogenic 10Be and in situ 14C. Quat.
886 Geochronol. 19, 14–26.
887 Ilyashuk, E.A., Koinig, K.A., Heiri, O., Ilyashuk, B.P., Psenner, R., 2011. Holocene temperature
888 variations at a high-altitude site in the Eastern Alps: a chironomid record from Schwarzsee
889 ob Sölden, Austria. Quat. Sci. Rev. 30, 176–191.
890 Ivy-Ochs, S., Kober, F., Alfimov, V., Kubik, P.W., Synal, H.-A., 2007. Cosmogenic ^{10}Be, ^{21}Ne
891 and ^{36}Cl in sanidine and quartz from Chilean ignimbrites. Nucl. Instrum. Methods Phys.
892 Res. B 259, 588–594.
893 Jost, A., Lunt, D., Kageyama, M., Abe-Ouchi, A., Peyron, O., Valdes, P.J., Ramstein, G., 2005.
894 High-resolution simulations of the last glacial maximum climate over Europe: a solution to
895 discrepancies with continental palaeoclimatic reconstructions? Clim. Dyn. 24, 577–590.

Kessler, M.A., Anderson, R.S., Stock, G.M., 2006. Modeling topographic and climatic control of east-west asymmetry in Sierra Nevada glacier length during the Last Glacial Maximum. Journal of Geophysical Research: Earth Surface 111.

Ketcham, R.A., 2005. Computational methods for quantitative analysis of three-dimensional features in geological specimens. Geosphere 1, 32–41.

Kuhlemann, J., Rohling, E.J., Krumrei, I., Kubik, P., Ivy-Ochs, S., Kucera, M., 2008. Regional synthesis of Mediterranean atmospheric circulation during the Last Glacial Maximum. Science 321, 1338–1340.

Larocque, I., Finsinger, W., 2008. Late-glacial chironomid-based temperature reconstructions for Lago Piccolo di Avigliana in the southwestern Alps (Italy). Palaeogeogr. Palaeoclimatol. Palaeoecol. 257, 207–223.

Liu, Z., Otto-Bliesner, B.L., He, F., Brady, E.C., Tomas, R., Clark, P.U., Carlson, A.E., Lynch-Stieglitz, J., Curry, W., Brook, E., Others, 2009. Transient simulation of last deglaciation with a new mechanism for Bølling-Allerød warming. Science 325, 310–314.

Loomis, S.E., Russell, J.M., Verschuren, D., Morrill, C., De Cort, G., Damsté, J.S.S., Olago, D., Eggermont, H., Street-Perrott, F.A., Kelly, M.A., 2017. The tropical lapse rate steepened during the Last Glacial Maximum. Science advances 3, e1600815.

Lovera, O.M., Grove, M., Mark Harrison, T., Mahon, K.I., 1997/8. Systematic analysis of K-feldspar $^{40}Ar/^{39}Ar$ step heating results: I. Significance of activation energy determinations. Geochim. Cosmochim. Acta 61, 3171–3192.

Lovera, O.M., Richter, F.M., 1989. The $^{40}Ar/^{39}Ar$ Thermochronometry for Slowly Cooled Samples. J. Geophys. Res. 94, 17–917.

Lovera, O.M., Richter, F.M., Harrison, T.M., 1991. Diffusion domains determined by ^{39}Ar

released during step heating. J. Geophys. Res. 96, 2057–2069.

Luetscher, M., Boch, R., Sodemann, H., Spötl, C., Cheng, H., Edwards, R.L., Frisia, S., Hof, F., Müller, W., 2015. North Atlantic storm track changes during the Last Glacial Maximum recorded by Alpine speleothems. Nat. Commun. 6, 6344.

Masson-Delmotte, V., Schulz, M., Abe-Ouchi, A., Beer, J., Ganopolski, A., González Rouco, J.F., Jansen, E., Lambeck, K., Luterbacher, J., Naish, T., Osborn, T., Otto-Bliesner, B., Quinn, T., Ramesh, R., Rojas, M., Shao, X., Timmermann, A., 2013. Information from paleoclimate archives, in: Stocker, T.F., Qin, D., Plattner, G.-K., Tignor, M., Allen, S.K., Boschung, J., Nauels, A., Xia, Y., Bex, V., Midgley, P.M. (Eds.), Climate Change 2013: The Physical Science Basis. Contribution of Working Group I to the Fifth Assessment Report of the Intergovernmental Panel on Climate Change. Cambridge University Press, Cambridge, United Kingdom, and New York, NY, USA, pp. 383–464.

McGreevy, J.P., 1985. Thermal properties as controls on rock surface temperature maxima, and possible implications for rock weathering. Earth Surf. Processes Landforms 10, 125–136.

Monegato, G., Scardia, G., Hajdas, I., Rizzini, F., Piccin, A., 2017. The Alpine LGM in the boreal ice-sheets game. Sci. Rep. 7, 2078.

Nishiizumi, K., Imamura, M., Caffee, M.W., Southon, J.R., Finkel, R.C., McAninch, J., 2007. Absolute calibration of ^{10}Be AMS standards. Nucl. Instrum. Methods Phys. Res. B 258, 403–413.

Schmidt, G.A., Annan, J.D., Bartlein, P.J., Cook, B.I., Guilyardi, E., Hargreaves, J.C., Harrison, S.P., Kageyama, M., LeGrande, A.N., Konecky, B., Lovejoy, S., Mann, M.E., Masson-Delmotte, V., Risi, C., Thompson, D., Timmermann, A., Tremblay, L.-B., Yiou, P., 2014. Using palaeo-climate comparisons to constrain future projections in CMIP5. Clim. Past 10,

221–250.

Schmittner, A., Urban, N.M., Shakun, J.D., Mahowald, N.M., Clark, P.U., Bartlein, P.J., Mix, A.C., Rosell-Melé, A., 2011. Climate sensitivity estimated from temperature reconstructions of the Last Glacial Maximum. Science 334, 1385–1388.

Schwarz, N., Schlink, U., Franck, U., Großmann, K., 2012. Relationship of land surface and air temperatures and its implications for quantifying urban heat island indicators--An application for the city of Leipzig (Germany). Ecol. Indic. 18, 693–704.

Shuster, D.L., Cassata, W.S., 2015. Paleotemperatures at the lunar surfaces from open system behavior of cosmogenic ^{38}Ar and radiogenic ^{40}Ar. Geochim. Cosmochim. Acta 155, 154–171.

Shuster, D.L., Farley, K.A., 2005. Diffusion kinetics of proton-induced ^{21}Ne, ^{3}He, and ^{4}He in quartz. Geochim. Cosmochim. Acta 69, 2349–2359.

Shuster, D.L., Farley, K.A., Sisterson, J.M., Burnett, D.S., 2004. Quantifying the diffusion kinetics and spatial distributions of radiogenic ^{4}He in minerals containing proton-induced ^{3}He. Earth Planet. Sci. Lett. 217, 19–32.

Stone, J.O., 2000. Air pressure and cosmogenic isotope production. J. Geophys. Res. [Solid Earth] 105, 23753–23759.

Tremblay, M.M., Shuster, D.L., Balco, G., 2014a. Cosmogenic noble gas paleothermometry. Earth Planet. Sci. Lett. 400, 195–205.

Tremblay, M.M., Shuster, D.L., Balco, G., 2014b. Diffusion kinetics of ^{3}He and ^{21}Ne in quartz and implications for cosmogenic noble gas paleothermometry. Geochim. Cosmochim. Acta 142, 186–204.

Tremblay, M.M., Shuster, D.L., Balco, G., Cassata, W.S., 2017. Neon diffusion kinetics and

965 implications for cosmogenic neon paleothermometry in feldspars. Geochim. Cosmochim.
966 Acta 205, 14–30.
967 Vermeesch, P., Baur, H., Heber, V.S., Kober, F., Oberholzer, P., Schaefer, J.M., Schlüchter, C.,
968 Strasky, S., Wieler, R., 2009. Cosmogenic ^{3}He and ^{21}Ne measured in quartz targets after
969 one year of exposure in the Swiss Alps. Earth Planet. Sci. Lett. 284, 417–425.
970 von der Heydt, A.S., Dijkstra, H.A., van de Wal, R.S.W., Caballero, R., Crucifix, M., Foster,
971 G.L., Huber, M., Köhler, P., Rohling, E., Valdes, P.J., Ashwin, P., Bathiany, S., Berends,
972 T., van Bree, L.G.J., Ditlevsen, P., Ghil, M., Haywood, A.M., Katzav, J., Lohmann, G.,
973 Lohmann, J., Lucarini, V., Marzocchi, A., Pälike, H., Baroni, I.R., Simon, D., Sluijs, A.,
974 Stap, L.B., Tantet, A., Viebahn, J., Ziegler, M., 2016. Lessons on Climate Sensitivity From
975 Past Climate Changes. Curr Clim Change Rep 2, 148–158.
976 Wu, H., Guiot, J., Brewer, S., Guo, Z., 2007. Climatic changes in Eurasia and Africa at the last
977 glacial maximum and mid-Holocene: reconstruction from pollen data using inverse
978 vegetation modelling. Clim. Dyn. 29, 211–229.

TABLES

Table 1: Locations and sample information for moraine boulders in the Gesso Valley previously exposure dated with cosmogenic ^{10}Be, originally reported in Federici et al. (2012, 2008).

Sample	Latitude (decimal degrees)	Longitude (decimal degrees)	Elevation (m)	Sample thickness (cm)	Shielding factor
PDP10	44.421534	7.819950	1806	3	0.9200
PM1	44.252667	7.385500	860	3	0.9653
PM4	44.252667	7.385500	860	3	0.9653
TDB1	44.289712	7.432528	770	3	0.9825
TDB3	44.289712	7.432528	770	3	0.9819

983 **Table 2:** Observations of cosmogenic ^{3}He in Gesso Valley quartz samples.

Sample - aliquot	Mass of quartz analyzed (g)	[^{3}He] (10^{6} atoms/g)		
PDP10-1	0.109	2.20	±	0.38
PDP10-2	0.101	2.38	±	0.37
PDP10-3	0.102	3.65	±	0.35
PDP10-4	0.126	2.91	±	0.26
PDP10-5	0.121	2.99	±	0.39
PDP10-6	0.136	2.99	±	0.31
PDP10-7	0.117	3.12	±	0.37
PDP10-8	0.125	2.44	±	0.35
PM1-1	0.101	1.14	±	0.42
PM1-2	0.101	0.89	±	0.6
PM1-3	0.304	1.11	±	0.18
PM1-4	0.266	0.88	±	0.15
PM1-5	0.290	1.05	±	0.15
PM4-1	0.113	1.29	±	0.34
PM4-2	0.309	1.51	±	0.17
PM4-3	0.268	1.63	±	0.19
PM4-4	0.247	1.60	±	0.12
TDB1-1	0.216	0.62	±	0.28
TDB1-2	0.269	0.11	±	0.14
TDB1-3	0.306	0.28	±	0.13
TDB1-4	0.292	0.26	±	0.13
TDB1-5	0.482	0.36	±	0.08
TDB3-1	0.216	1.38	±	0.27
TDB3-2	0.124	1.35	±	0.39
TDB3-3	0.279	1.20	±	0.19
TDB3-4	0.301	1.31	±	0.27
TDB3-5	0.268	1.32	±	0.18

984

985 **Table 3:** Apparent ^{3}He exposure ages and retention in Gesso Valley quartz samples. See text for
986 details about the input parameters to the exposure age calculation. Because we have
987 measurements of cosmogenic ^{3}He from multiple aliquots of each sample, we report weighted
988 mean apparent exposure ages with internal uncertainties alongside weighted mean apparent
989 exposure ages with external uncertainties in parentheses. Because we only have one ^{10}Be
990 measurement per sample, we report a single ^{10}Be exposure age for each sample with internal
991 uncertainty alongside external uncertainty in parentheses. Cosmogenic ^{3}He retention is
992 calculated using external uncertainties.

Sample	Weighted mean apparent exposure age (yr), ^{3}He	Exposure age (yr), ^{10}Be	^{3}He retention		
PDP10	6513 ± 273 (6402 ± 341)	14071 ± 606(1220)	0.46	±	0.05
PM1	4539 ± 400 (4534 ± 452)	16356 ± 1023(1601)	0.28	±	0.04
PM4	7071 ± 377 (7006 ± 512)	19213 ± 799(1654)	0.36	±	0.04
TDB1	1424 ± 261 (1407 ± 271)	23397 ± 1085(2072)	0.06	±	0.01
TDB3	6178 ± 496 (6187 ± 561)	21003 ± 965(1854)	0.29	±	0.04

993

994 **Table 4:** Three domain multiple diffusion domain model parameters for ^{3}He diffusion
995 experiments in Gesso Valley quartz samples.

Experiment	Domain	E_a (kJ/mol)	$\ln(D_0/a^2)$	fraction	Misfit
PDP10-B	1	96.5	10.2	0.61	0.097
	2		16.1	0.21	
	3		13.2	0.18	
PM1-A	1	89.6	8.6	0.54	0.067
	2		10.1	0.36	
	3		14.1	0.1	
PM4-A	1	90.9	8.4	0.74	0.109
	2		5.9	0.2	
	3		14.4	0.06	
TDB1-B	1	99.7	11.8	0.46	0.161
	2		13.2	0.3	
	3		17.3	0.24	
TDB3-B	1	97.6	10.3	0.42	0.149
	2		12.3	0.41	
	3		15.7	0.17	

996

997 **FIGURES**

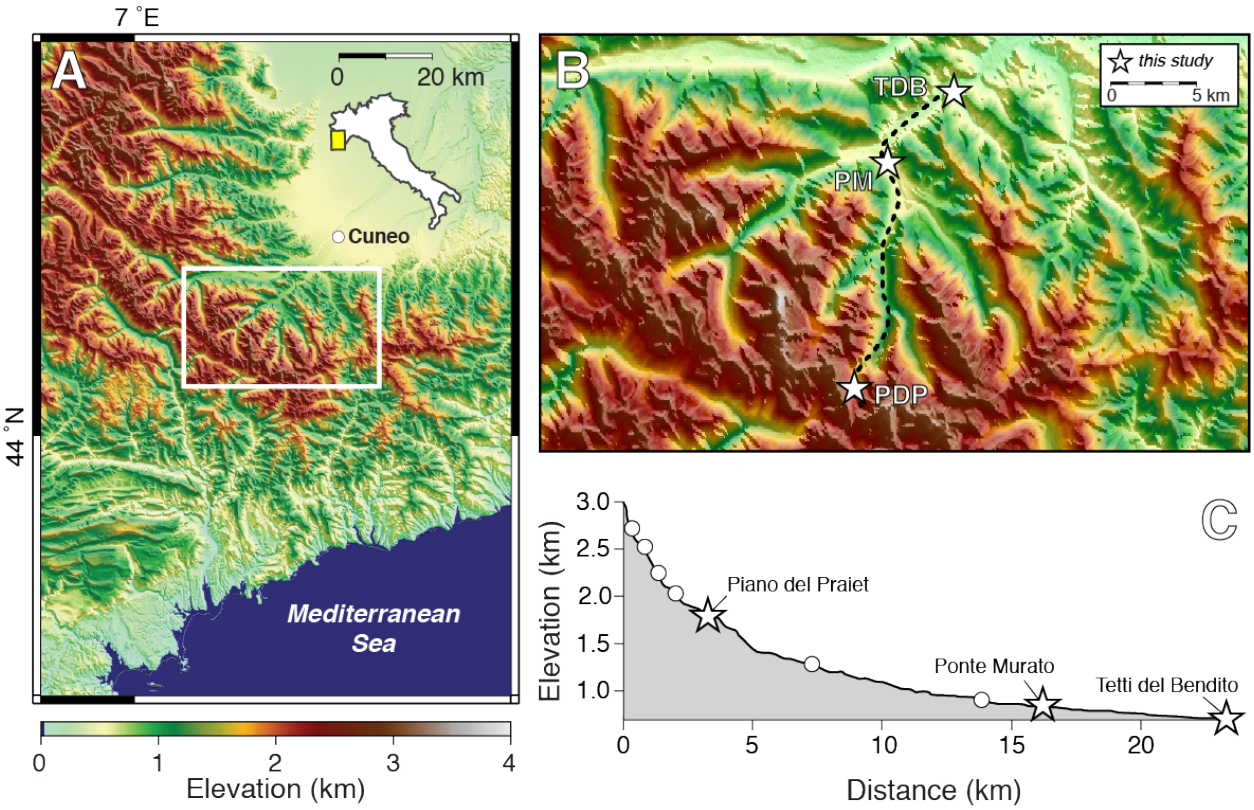

Figure 1: A: Topographic map of the Maritime Alps. Map location is shown in the inset of Italy. White box corresponds to the enlarged view in (B). B: Topography of the Gesso Valley. White stars mark the locations of moraines sampled for this study: Piano del Praiet (PDP), Ponte Murato (PM), and Tetti del Bandito (TDB). Dashed line corresponds to the longitudinal profile shown in (C). C: Longitudinal profile of the Gesso Valley. White stars mark the locations of moraines studied here, as in (B); white circles denote additional moraines in the Gesso Valley not studied here. A detailed map of the geomorphic features in the Gesso Valley is available in Federici et al. (2003).

998

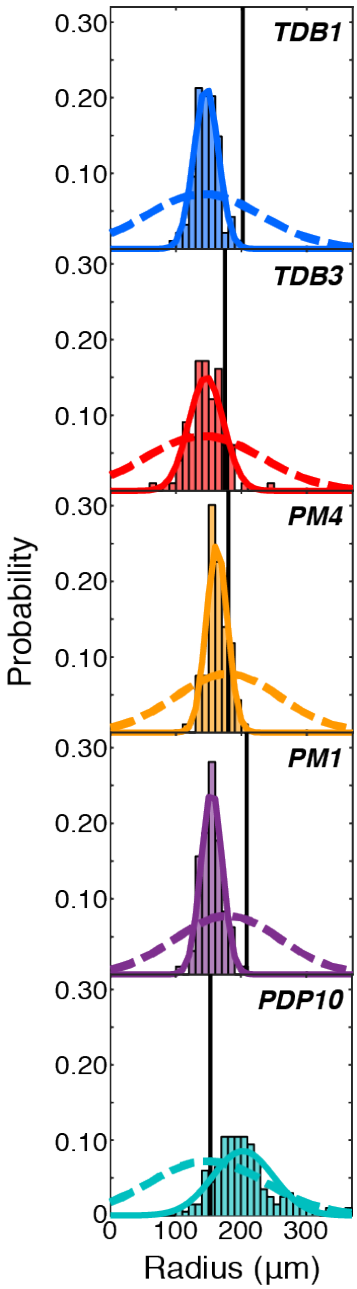

Figure 2: Grain size analysis for Gesso Valley samples. Histograms and solid curves denote the distribution of spherical equivalent radii for representative quartz grains (≥100) from the sieve fraction analyzed for cosmogenic ^{3}He abundances. Dashed curves denote the distribution of spherical equivalent radii in whole rock, inverted from the distribution of sectional circles of quartz grains (≥100) measured in thin section. Thin sections were made from the same sample as the crushed fraction, in the case of PDP10, or from a resampled boulder on the same moraine, in all other cases. Vertical black lines denote the spherical equivalent radius of the single quartz grain analyzed in each diffusion experiment shown in Fig. 4.

999

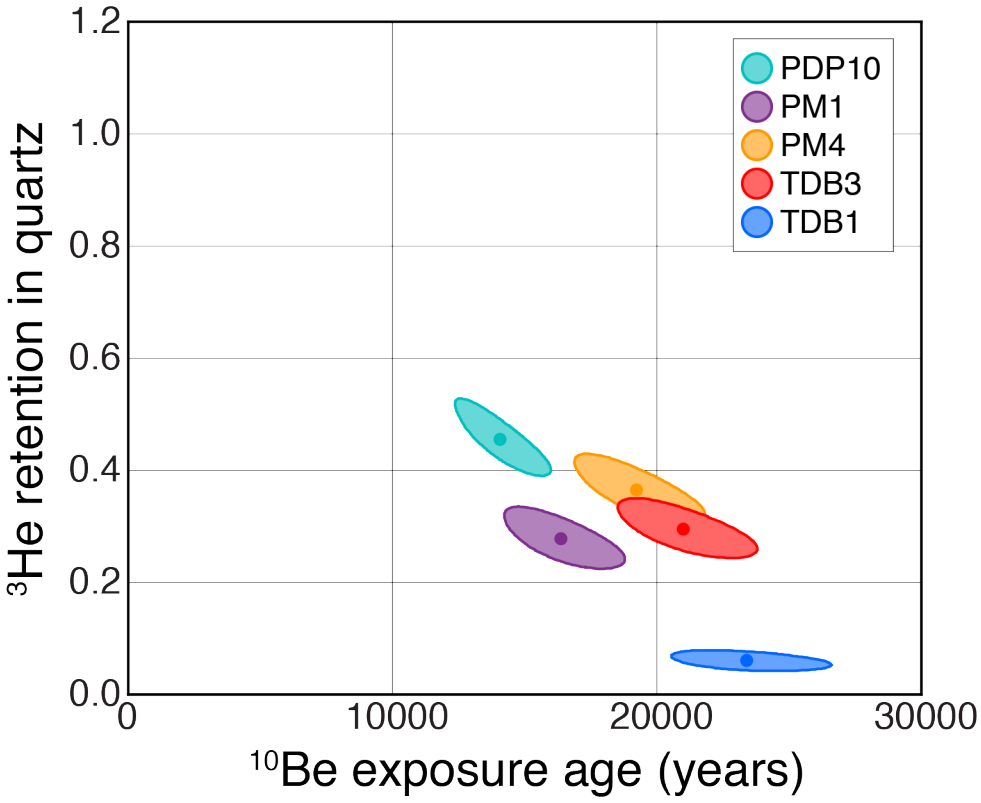

Figure 3: Cosmogenic ^{3}He retention as a function of ^{10}Be exposure age in quartz from Gesso Valley moraine samples. Ellipses represent 1σ uncertainty.

1000

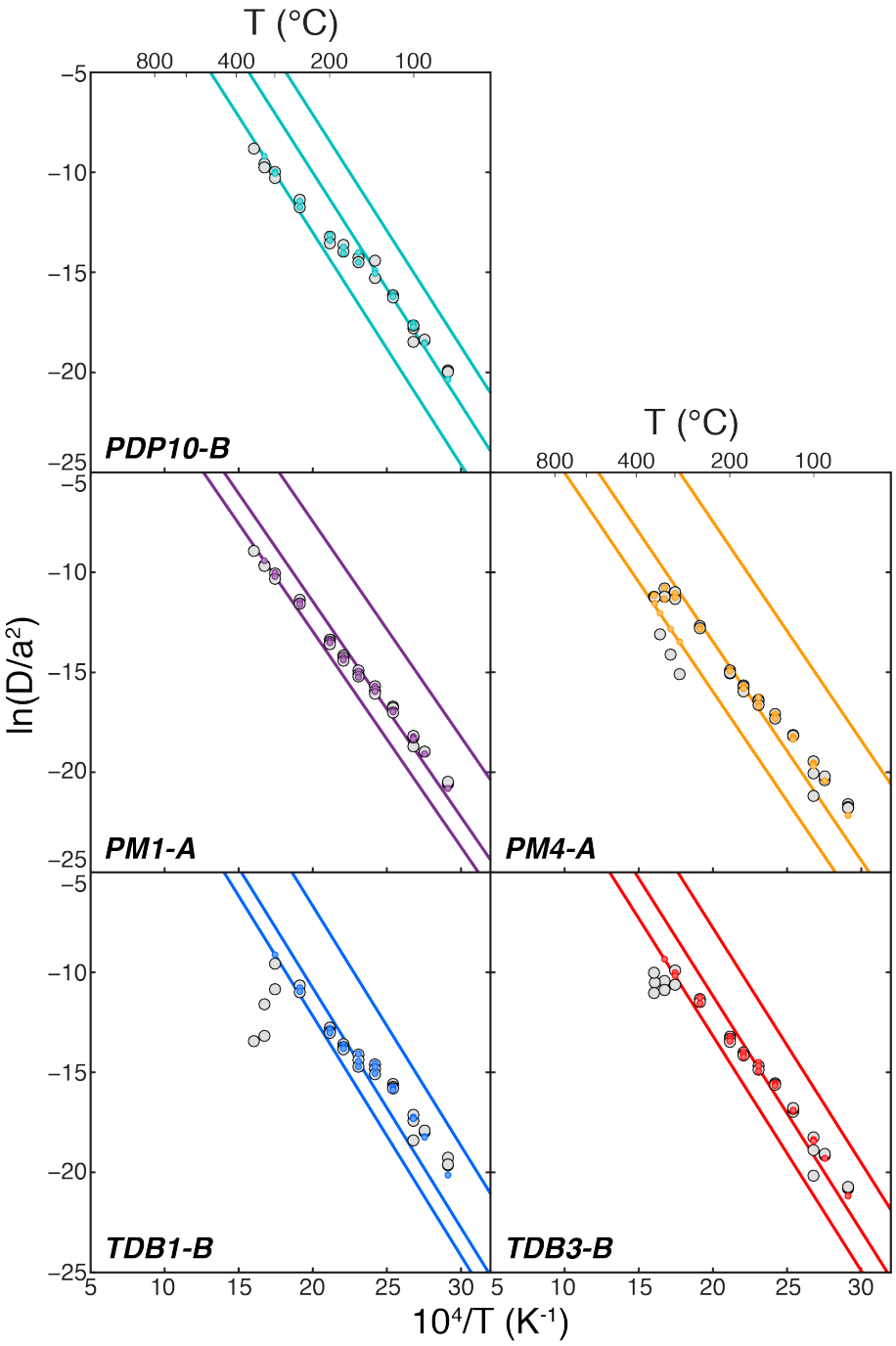

Figure 4: Arrhenius plots for helium diffusion experiments on Gesso Valley quartz samples. D/a^2 values are normalized to s^{-1}. Experimental data are plotted as gray circles. Diffusivities were calculated using the equations of Fechtig and Kalbitzer (1966) and the uncertainty propagation outlined in Tremblay et al. (2014b). Color circles and lines denote three-domain multiple diffusion domain (MDD) models that minimize misfit with the experimental data. Tremblay et al. (2017) describe MDD modeling approach used here.

1001

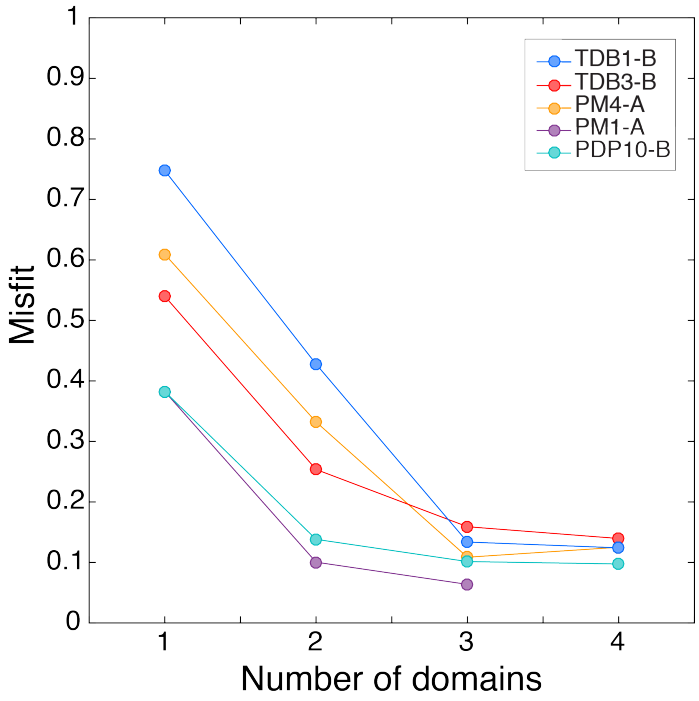

Figure 5: Minimized misfit between observed and MDD-modeled ^{3}He diffusivities as a function of number of diffusion domains for Gesso Valley quartz samples. We increased the number of diffusion domains in our MDD models until the addition of another diffusion domain did not significantly reduce the misfit between the observed and calculated diffusivities. For all Gesso Valley quartz samples, we found that increasing the number of domains from three to four only marginally improved the misfit; therefore we use three-domain MDD models in subsequent calculations. For experiment PM1-A, attempts at constructing a four domain model yielded two domains with the same pre-exponential factor and thus are the equivalent of the three domain model.

1002

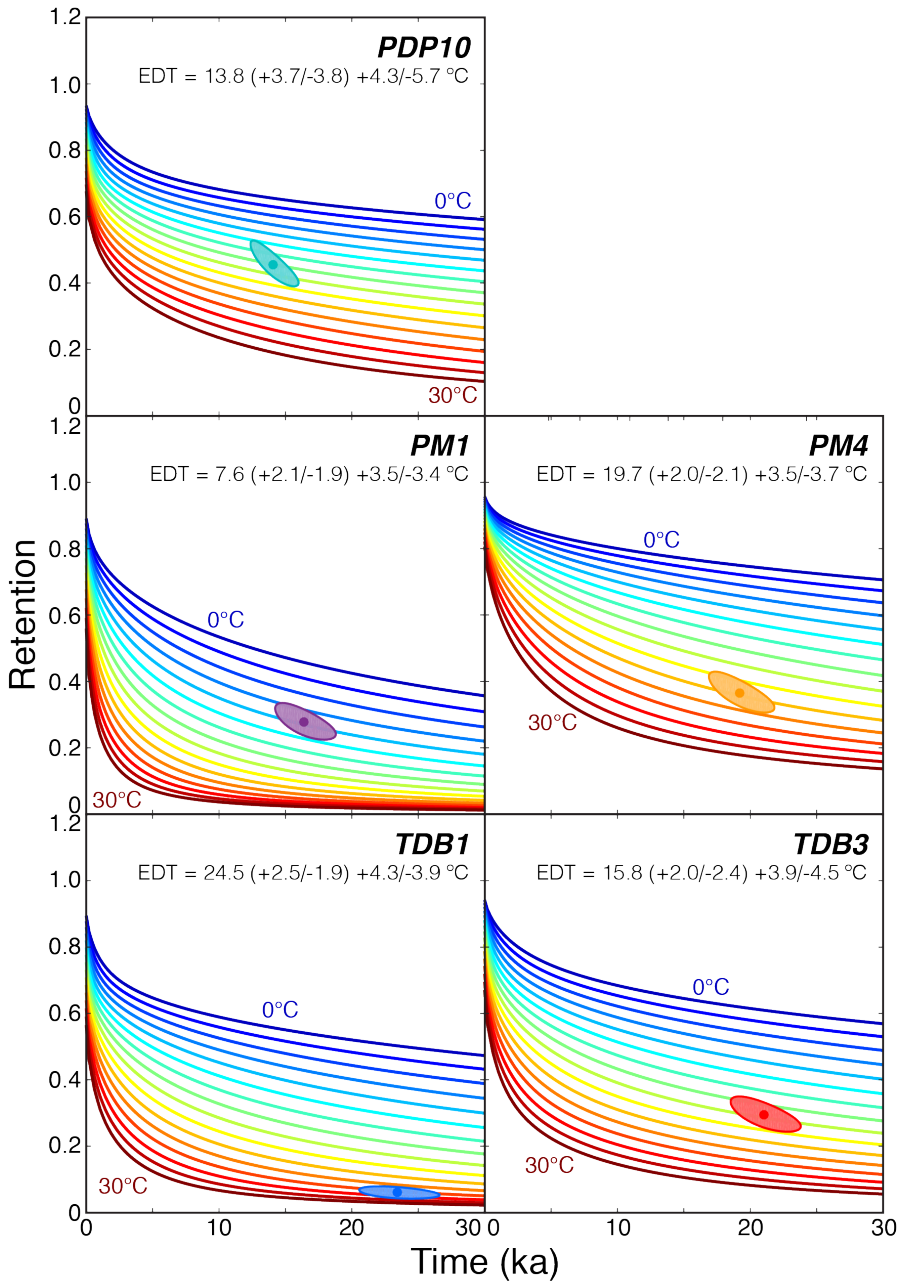

Figure 6: EDTs integrated over the exposure duration of Gesso Valley moraine samples. For each sample, we plot cosmogenic ^{3}He retention as a function of exposure duration for constant EDTs ranging from 0 to 30 ºC in 2 ºC increments, and assuming the MDD model diffusion kinetics reported in Table 3. Observed cosmogenic ^{3}He retention ellipses are plotted as in Fig. 4 for comparison. One σ EDT uncertainties in parentheses account for the uncertainty in ^{3}He retention and exposure duration as determined from ^{10}Be measurements; the second set of uncertainties account for uncertainty in the spherical equivalent radius to which the experimentally-determined diffusion kinetics are scaled in addition to the uncertainties in ^{3}He retention and exposure duration.

1003

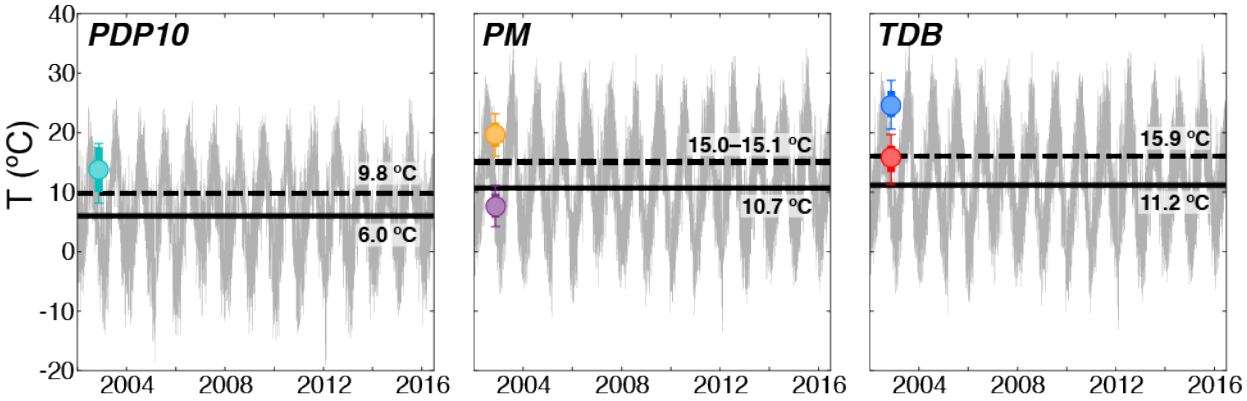

Figure 7: EDTs calculated from modern meteorological data. In gray we show the time series of mean, minimum, and maximum daily temperatures from 2002 to mid-2016 at the elevations of the PDP, PM, and TDB moraines, scaled from the nearest two meteorological stations using average monthly lapse rates. Solid black bars denote the mean temperature for each time series; dashed black bars denote the modern EDT for each time series calculated using the activation energies of the best fit MDD models in Fig. 4 and Table 4. EDTs integrated over the exposure duration of each sample are also shown for comparison as circles, with colors for specific samples and 1σ uncertainties as reported in Fig. 6.

1004

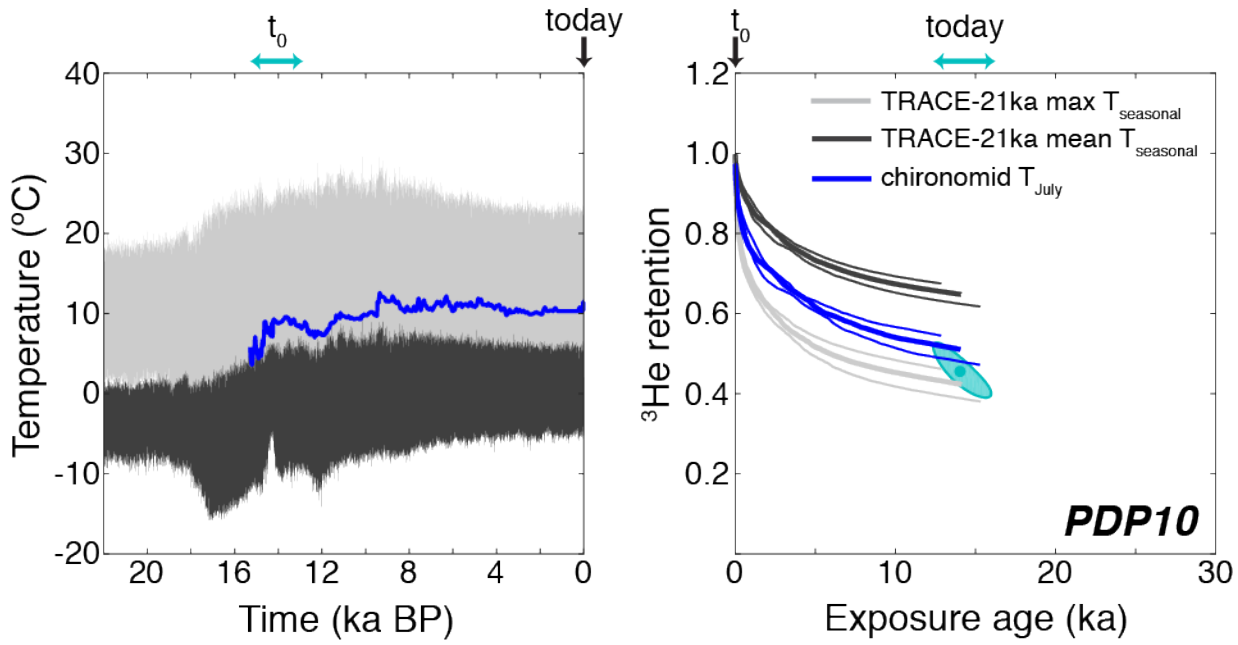

Figure 8: Cosmogenic ^{3}He retention in PDP10 quartz calculated from scaled TraCE-21ka seasonal temperatures and scaled, spliced chironomid July temperatures. The left panel shows the mean (black) and maximum (gray) seasonal temperature from the TraCE-21ka climate simulation and the mean July temperature (blue) from four spliced chironomid records, scaled to the elevation of PDP10 using modern lapse rate data and, for the chironomid records, weighted by distance from our study site. The right panel shows the evolution of ^{3}He retention with time assuming the TraCE-21ka and chironomid temperatures represent the EDT experience over PDP10's exposure duration. Thick retention curves assume the mean exposure duration and grain size for diffusion kinetics scaling; lower thin retention curves assume the +1σ exposure duration and grain size, while upper thin curves assume the –1σ exposure duration and grain size. The ellipse shows the observed retention and exposure duration, as in Fig. 3.

1005

1006

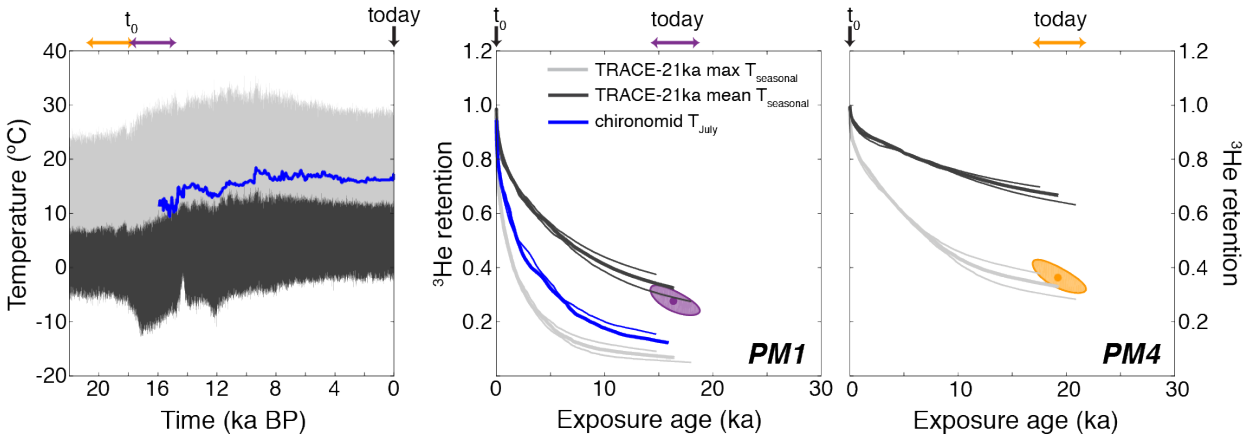

Figure 9: Cosmogenic ^{3}He retention in PM1 and PM4 calculated from scaled TraCE-21ka seasonal temperatures and, in the case of PM1, scaled, spliced chironomid July temperatures. The left panel shows the mean (black) and maximum (gray) seasonal temperature from the TraCE-21ka climate simulation and the mean July temperature (blue) from four spliced chironomid records, scaled to the elevation of PM using modern lapse rate data and, for the chironomid records, weighted by distance from our study site. The right panels show the evolution of ^{3}He retention with time assuming the TraCE-21ka and chironomid temperatures represent the EDT experience over the PM samples' exposure duration. Thick and thin retention curves are as in Fig. 8. Ellipses show the observed retention and exposure duration, as in Fig. 3.

1007

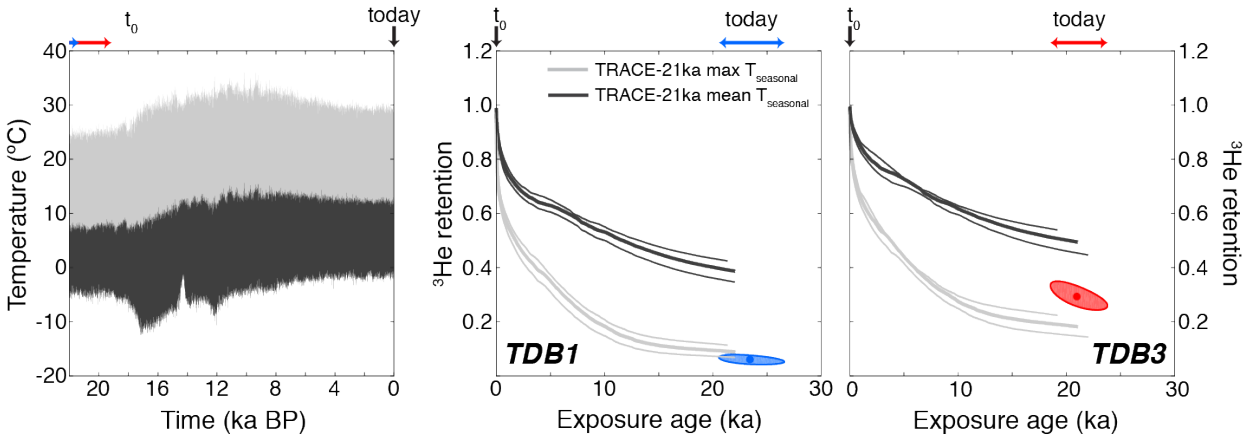

Figure 10: Cosmogenic ^{3}He retention calculated in TDB1 and TDB3 from scaled TraCE-21ka seasonal temperatures. The left panel shows the mean and maximum seasonal temperature from the TraCE-21ka climate simulation, scaled to the elevation of the TDB moraine using modern lapse rate data. The right panels shows the evolution of ^{3}He retention with time assuming the TraCE-21ka temperatures represent the EDT experience over the TDB samples' exposure duration. Thick and thin retention curves are as in Fig. 8. Ellipses show the observed retention and exposure duration, as in Fig. 3.

1008

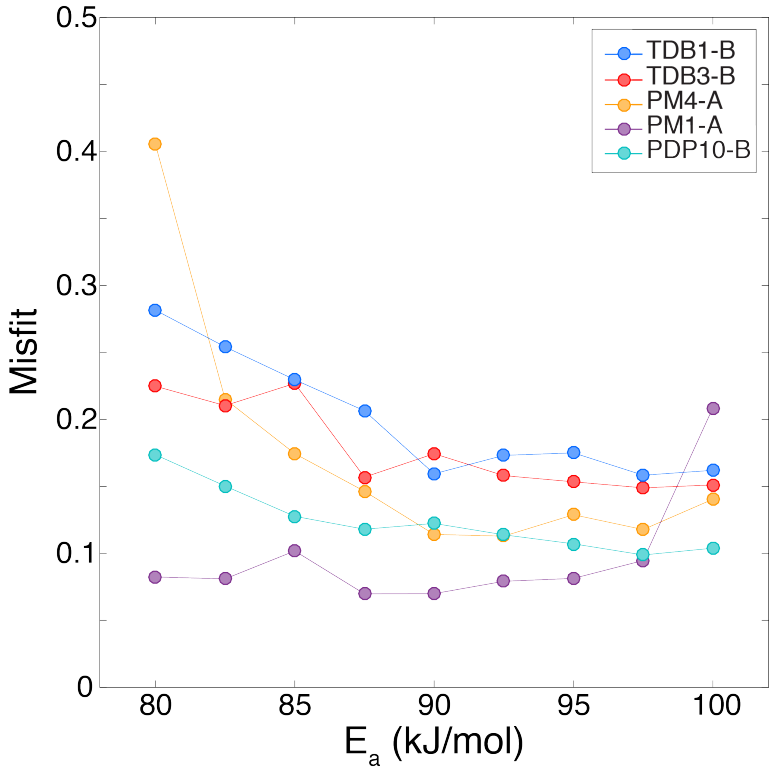

Figure 11: Minimized misfit between observed and MDD-modeled ^{3}He diffusivities as a function of activation energy E_a for Gesso Valley quartz samples, assuming a three domain diffusion model. Pre-exponential factors and gas fractions for each domain covary with E_a; we show misfit as a function of E_a because it is assumed to be common to all diffusion domains in our modeling approach.

1009